

Full length article

Discrete Kirchhoff–Love shell quadrilateral finite element designed from cubic Hermite edge curves and Coons surface patch

Tomo Veldin^a, Boštjan Brank^{b,*}, Miha Brojan^a^a University of Ljubljana, Faculty of Mechanical Engineering, Laboratory for Nonlinear Mechanics, Aškerčeva 6, SI-1000, Ljubljana, Slovenia^b University of Ljubljana, Faculty of Civil and Geodetic Engineering, Jamova 2, SI-1000, Ljubljana, Slovenia

ARTICLE INFO

Keywords:

Discrete Kirchhoff–Love shell quadrilateral finite element
Cubic Hermite curve
Bilinear Coons patch
 G^1 -continuity

ABSTRACT

We present a nonlinear discrete Kirchhoff–Love four-node shell finite element that is based on the cubic Hermite edge curves and the bilinear Coons surface patch spanning the surface between them. The cubic Hermite edge curves are constructed by minimizing the bending curvature of a spatial curve connecting two adjacent nodes of the element. The G^1 -continuity is obtained at each node of the finite element mesh. Namely, the tangent vectors of the set of the edge curves attached to a given node of the mesh share the same tangent plane to the shell mid-surface for any configuration. To avoid the membrane locking, common in shell elements with higher-order interpolations, the assumed natural strains are adopted, solving the plate compatibility equation. The derived element has 5 degrees of freedom per node, 3 mid-surface displacements and 2 rotations of the mid-surface normal vector, which also rotate the corresponding mid-surface tangent plane. Several numerical examples illustrate its performance in linear and nonlinear tests, for both regular and distorted meshes.

1. Introduction

Curvature-induced high ratio between the load-bearing capacity and weight, as well as the aesthetic features, make shell structures invaluable in many engineering and technological applications, ranging from cooling towers, roofs, containers, ship hulls, aircraft fuselages, car bodies, to thin-walled smart memory alloys and nano-shells. The shell can be geometrically represented as an intrinsic 2D curved surface with prescribed thickness. Taking this into account, the mathematical description of shell deformation and motion under external loadings becomes much more complex than the corresponding description for the 3D solid. There are various shell theories in use that are based on different assumptions and therefore applicable for different types of shells (e.g. thick, thin, shallow, axisymmetric, etc.) and different types of shell behaviour (e.g. linear, geometrically non-linear, inelastic, etc.). Commonly used shell theories that differ in terms of the basic kinematic assumption are the theory with the Reissner–Mindlin kinematics (which accounts for transverse shear deformation energy), the Kirchhoff–Love theory (for thin shells), the Donnell–Mustari–Vlasov theory (for thin and shallow shells), the solid-shell theory (useful for shells with complex (inelastic) material behaviour), and the multi-layered shell theory.

As for the finite element approximations, the shell theory with the Reissner–Mindlin kinematics requires only C^0 -continuity for the functions that approximate the initial and deformed shell geometries,

e.g. [1–5]. In contrast, the Kirchhoff–Love shell theory requires C^1 -continuity of the corresponding functions, which is incredibly hard to achieve, and requires, among other complexities, a large number of element's degrees of freedom, e.g. [6,7].

In the computer graphics and geometric modelling, the surface patches are used for the representation of curved surfaces, e.g. [8]. In general, it is possible to achieve different levels of continuity/smoothness between surface patches, with the C^1 -continuity being much more difficult to achieve than the G^1 -continuity. Indeed, the C^1 -continuity between two adjacent surface patches requires a unique tangent plane to the surface at any point of the common boundary, and that the patches have identical parametric tangent vectors that are members of the tangent plane. The G^1 -continuity is less strict and does not require the same length of the tangent vectors. By definition, the two patches with a common boundary are G^1 -continuous if they have a continuously varying tangent plane along that boundary. There are several surface patches available, e.g. [8]. The most basic is the bi-linearly blended Coons patch, followed by the partially bi-cubically blended Coons and bi-cubically blended Coons patches. The shapes of these patches are controlled by the nodal points, boundary curves and corner twist. Another type of the surface patches are the Bezier patches, the shapes of which are defined by control points: the degree of the Bezier patch corresponds to the number of control points. Similar to the Bezier surface patches are the B-splines, the shapes of which are also

* Corresponding author.

E-mail address: Boštjan.Brank@fgg.uni-lj.si (B. Brank).

controlled by control points and can be written in a piecewise Bezier form. Extensions of the B-splines are NURBS (non-uniform rational basis splines) and T-splines (e.g. [9]), which also fall into the category of NURBS.

Some of the above mentioned surface patches were used for the derivation of plate and shell finite elements. For example, in [10], the Coons-Gregory surface patch, which is an extension of the bi-cubic Coons patch, was used for interpolating the transverse displacement of a linear quadrilateral Kirchhoff plate finite element. In [11], the deformed geometry of a linear quadrilateral plate finite element was interpolated with the Gregory patch, which is an extension of the rational bi-cubic Bezier surface patch. The Kirchhoff plate finite elements based on the Gregory surface patch guarantee the G^1 -continuity of the transverse displacement between the elements, but not the continuity of its second derivatives, which causes the related plate elements to fail the (bending) patch test if constraints are not enforced, see [11]. The ideas from [10] and [11] were applied to linear shells in [7]. As for the shell finite elements, many recently proposed formulations are based on the approach of isogeometric analysis (IGA) introduced by Hughes [12], see e.g. Kiendl et al. [13]. The main idea behind the IGA formulations is to use the computer aided design functions to define the finite element approximations. The isogeometric shell finite elements use B-splines and NURBS to interpolate any shell configuration with high degree of continuity. The problem of G^1 -continuity between adjacent patches appears also in isogeometric shell formulations. To this end, Kiendl et al. [14] introduced a penalty formulation based on the bending strip method, which was later accompanied by several other strategies to enforce the G^1 -continuity between the patches.

The discrete Kirchhoff plate and the discrete Kirchhoff-Love shell finite elements satisfy the continuity requirements only at the discrete boundary points and not along the entire boundary of the element. In the majority of formulations, the continuity requirements are imposed implicitly by enforcing the Kirchhoff kinematic constraint at the discrete boundary points. For example, the linear discrete Kirchhoff quadrilateral plate elements from [15–17] enforce the Kirchhoff kinematic constraint at the nodes (and partly along each edge in the direction of the edge). For a review of linear discrete Kirchhoff plate and discrete Kirchhoff-Love shell finite elements, we refer the reader to [18]. As for the geometrically non-linear (large rotation) discrete Kirchhoff-Love shell finite elements, most formulations are for triangles, and only a few for quadrilaterals, see [19–21]. In [20], the integral form for zero transverse shear strains along the element edges (in the direction of the edge) is enforced, and in [21], the Kirchhoff-Love constraints are imposed at mid-sides of the edges of the element with a non-standard numerical quadrature.

This work presents a novel discrete Kirchhoff-Love non-linear (large rotation) quadrilateral finite element. The formulation is based on the bilinear Coons patch spanned between the cubic Hermite edge curves. The tangent vectors at both ends of the Hermite edge curve lie on the tangent planes to the mid-surface of the shell, which provides the G^1 -continuity in the nodes. The derived element has only 5 degrees of freedom per node, i.e. 3 displacements and 2 rotations, which is much less than full Kirchhoff-Love shell formulations, e.g. [6,7]. The rotational degrees of freedom rotate the nodal mid-surface normal vector along with the corresponding tangent plane to the mid-surface of the shell. This, together with the displacement degrees of freedom, affects the shapes of the Hermite edge curves and the Coons surface patch, but keeps the G^1 -continuity in the nodes for any shell configuration. In this way, we manage to keep the same number of the degrees of freedom as required for the corresponding quadrilaterals with the Reissner-Mindlin kinematics, which have much lower continuity requirement between elements. Moreover, the same data as for the Reissner-Mindlin elements is needed to construct the mesh for the derived discrete Kirchhoff-Love element: nodal coordinates and mid-surface normals. The proposed element can also be modified for analysis of non-smooth shells with kinks. The technique, which is

frequently used for 5 dofs/node Reissner-Mindlin shell finite elements (with 2 local rotational dofs/node), e.g. [22], fits the proposed element as well.

The derived finite element has higher-order interpolation functions, which are capable to describe curved shell geometries more accurately. A disadvantage of such higher-order interpolation is strong membrane locking. The bending deformations are accompanied by parasitic membrane strains that artificially stiffen the element. In order to eliminate the membrane locking, we use the assumed natural strain (ANS) method as proposed in [3].

Section 2 of the paper introduces the basics of the Kirchhoff-Love theory, followed by the definition of the edge curves of the finite element in Section 3, and the definition of the finite element surface via the Coons patch in Section 4. Section 5 describes the applied ANS method for membrane locking, a set of numerical examples is presented in Section 6, and conclusions are drawn in Section 7. Some additional derivations, longer expressions and interpolation functions are given in Appendix.

2. Shell theory

The Kirchhoff-Love shell theory assumes that the normal vector to the initial middle surface of the shell remains normal also in the deformed configuration. This assumption implies the neglect of the transverse shear deformation energy and allows to describe the geometry of the initial and the deformed configuration of the shell in exactly the same manner.

In order to distinguish between the initial and the deformed configuration, we denote the objects of the former by upper case letters and the objects of the latter by lower case letters. For the indices, we adopt the standard notation (with some exceptions) using small Greek letters for indices 1,2 and small Latin letters for indices 1, 2, 3.

2.1. Kinematics

Let the undeformed (initial) shell configuration S be described in \mathbb{R}^3 as:

$$\bar{X}(\xi^1, \xi^2, \xi^3) := X(\xi^1, \xi^2) + \xi^3 \mathbf{A}_3(\xi^1, \xi^2), \quad (1)$$

where $(\xi^1, \xi^2) \in \mathcal{A} \subset \mathbb{R}^2$ and $\xi^3 \in [-h/2, h/2] \subset \mathbb{R}$ represent a triplet of curvilinear coordinates. Hereinafter, for the sake of brevity, we will omit writing the arguments of the function. Thus, X describes the mid-surface M , \mathbf{A}_3 is the unit vector field that is normal to M , \mathcal{A} is a parametrization domain of M , and h is the initial thickness of the shell (constant in our case). The tangent plane on M , denoted by \mathcal{T}_M , is defined by the vectors

$$\mathbf{A}_\alpha := X_{,\alpha} =: \frac{\partial X}{\partial \xi^\alpha}, \quad \alpha \in \{1, 2\}, \quad (2)$$

which, together with

$$\mathbf{A}_3 := \frac{\mathbf{A}_1 \times \mathbf{A}_2}{\|\mathbf{A}_1 \times \mathbf{A}_2\|}, \quad (3)$$

form a local covariant basis. Because \mathbf{A}_3 is perpendicular to M and because of unit length, the following holds:

$$\mathbf{A}_\alpha \cdot \mathbf{A}_3 = 0, \quad \mathbf{A}_{3,\alpha} \cdot \mathbf{A}_3 = 0, \quad \mathbf{A}_3 \cdot \mathbf{A}_3 = 1 \quad \text{and} \quad \mathbf{A}^3 = \mathbf{A}_3. \quad (4)$$

The contravariant basis vectors \mathbf{A}^i are defined by the orthogonality condition $\mathbf{A}^i \cdot \mathbf{A}_j = \delta_j^i$, where δ_j^i is the Kronecker delta symbol. In a point on S , a local covariant basis is constructed as:

$$\mathbf{G}_\alpha = \mathbf{A}_\alpha + \xi^3 \mathbf{A}_{3,\alpha} \quad \text{and} \quad \mathbf{G}_3 = \mathbf{A}_3. \quad (5)$$

The covariant elements $G_{ij} := \mathbf{G}_i \cdot \mathbf{G}_j$ of the metric tensor G are

$$G_{\alpha\beta} = A_{\alpha\beta} - 2\xi^3 B_{\alpha\beta} + (\xi^3)^2 C_{\alpha\beta}, \quad G_{\alpha 3} = 0, \quad G_{33} = 1, \quad (6)$$

where $A_{\alpha\beta}$, $B_{\alpha\beta}$ and $C_{\alpha\beta}$ represent the covariant elements of the first, second and third fundamental forms of the mid-surface M , respectively. They are defined as:

$$A_{\alpha\beta} := \mathbf{A}_\alpha \cdot \mathbf{A}_\beta, \quad B_{\alpha\beta} := \mathbf{A}_3 \cdot \mathbf{A}_{\alpha\beta}, \quad C_{\alpha\beta} := \mathbf{A}_{3,\alpha} \cdot \mathbf{A}_{3,\beta}. \quad (7)$$

The initial and the deformed mid-surface are connected by the displacement field \mathbf{U}

$$\mathbf{x} = \mathbf{X} + \mathbf{U}. \quad (8)$$

Because of the Kirchhoff–Love kinematic assumption, the structure of the above kinematic expressions, given for the initial configuration, remains the same also for the deformed configuration.

For the strain measure, we will use the Green–Lagrange strain tensor

$$\mathbf{E} := \frac{1}{2}(\mathbf{g} - \mathbf{G}), \quad (9)$$

where \mathbf{g} denotes the metric tensor of the deformed shell configuration s . Because of the same structure of the kinematic expressions in the initial and deformed configuration, as mentioned above, we can write the components of the Green–Lagrange strain tensor in terms of to the contravariant basis $\mathbf{A}^\alpha, \mathbf{A}^3$ as

$$E_{\alpha\beta} = \epsilon_{\alpha\beta} + \xi^3 \kappa_{\alpha\beta} + (\xi^3)^2 \rho_{\alpha\beta}, \quad \text{and} \quad E_{i3} = 0, \quad (10)$$

where

$$\epsilon_{\alpha\beta} = \frac{1}{2}(a_{\alpha\beta} - A_{\alpha\beta}), \quad \kappa_{\alpha\beta} = -(b_{\alpha\beta} - B_{\alpha\beta}), \quad \rho_{\alpha\beta} = \frac{1}{2}(c_{\alpha\beta} - C_{\alpha\beta}), \quad (11)$$

and $a_{\alpha\beta}, b_{\alpha\beta}$ and $c_{\alpha\beta}$ are the fundamental forms of the deformed mid-surface m . Following the usual approach, such as e.g. in [23], we will neglect the effect of $\rho_{\alpha\beta}$.

To conclude this section, let us recall some useful identities from the differential geometry, see e.g. [24], that apply for the adopted shell theory (summation over repeated indices applies):

$$\mathbf{A}_{3,\alpha} = -B_\alpha^\gamma \mathbf{A}_\gamma, \quad B_\alpha^\gamma \mathbf{A}_{\gamma\beta} = B_{\alpha\beta}, \quad B_\alpha^\gamma B_{\gamma\beta} = C_{\alpha\beta}, \quad (12)$$

$$\mathbf{A}_1 \times \mathbf{A}_2 = \sqrt{A} \mathbf{A}_3, \quad \mathbf{A}_2 \times \mathbf{A}_3 = \sqrt{A} \mathbf{A}^1, \quad \mathbf{A}_3 \times \mathbf{A}_1 = \sqrt{A} \mathbf{A}^2, \quad (13)$$

$$A = \|\mathbf{A}_1 \times \mathbf{A}_2\|^2 = A_{11}A_{22} - (A_{12})^2, \quad \mathbf{A}^\alpha = A^{\alpha\gamma} \mathbf{A}_\gamma, \quad A^{\alpha\gamma} A_{\gamma\beta} = \delta_\beta^\alpha, \quad (14)$$

$$\Gamma_{\alpha\beta}^\gamma = \mathbf{A}^\gamma \cdot \mathbf{A}_{\alpha,\beta} = -\mathbf{A}_\beta \cdot \mathbf{A}_{\alpha,\gamma}. \quad (15)$$

2.2. Constitutive relations

We will use the thin-shell version of the isotropic St. Venant–Kirchhoff hyperelastic strain energy function, which is appropriate for large displacements and rotations, but only for moderately large strains. It takes into account the plane stress assumptions, and it is defined as a sum of two parts, $W = {}_0W + {}_1W$, where ${}_0W$ is the membrane deformation energy density and ${}_1W$ is the bending deformation energy density. For the chosen strain energy function, the second Piola–Kirchhoff membrane forces and bending moments are its energy conjugates. They are given as:

$$N^{\alpha\beta} = \frac{\partial {}_0W}{\partial \epsilon_{\alpha\beta}} = \frac{Eh}{1-\nu^2} H^{\alpha\beta\gamma\delta} \epsilon_{\gamma\delta}, \quad (16)$$

$$M^{\alpha\beta} = \frac{\partial {}_1W}{\partial \kappa_{\alpha\beta}} = \frac{Eh^3}{12(1-\nu^2)} H^{\alpha\beta\gamma\delta} \kappa_{\gamma\delta},$$

where E is Young’s modulus, ν is Poisson’s ratio and $H^{\alpha\beta\gamma\delta}$ are the components of the isotropic constitutive tensor

$$H^{\alpha\beta\gamma\delta} = \nu A^{\alpha\beta} A^{\gamma\delta} + \frac{1}{2}(1-\nu)(A^{\alpha\gamma} A^{\beta\delta} + A^{\alpha\delta} A^{\beta\gamma}). \quad (17)$$

By using Voigt’s notation for the strains and stress resultants,

$$\boldsymbol{\epsilon} = [\epsilon_{11}, \epsilon_{22}, 2\epsilon_{12}]^T, \quad \boldsymbol{\kappa} = [\kappa_{11}, \kappa_{22}, 2\kappa_{12}]^T, \quad (18)$$

$$\mathbf{N} = [N^{11}, N^{22}, N^{12}]^T, \quad \mathbf{M} = [M^{11}, M^{22}, M^{12}]^T, \quad (19)$$

we obtain the following relations from Eqs. (16) and (17):

$$\mathbf{N} = \frac{Eh}{1-\nu^2} \mathbf{H} \boldsymbol{\epsilon}, \quad \mathbf{M} = \frac{Eh^3}{12(1-\nu^2)} \mathbf{H} \boldsymbol{\kappa}, \quad (20)$$

where the constitutive matrix \mathbf{H} is (see e.g. [23]):

$$\mathbf{H} = \begin{bmatrix} A^{11} A^{11} & \nu A^{11} A^{22} + (1-\nu) A^{12} A^{12} & A^{11} A^{12} \\ \nu A^{11} A^{22} + (1-\nu) A^{12} A^{12} & A^{22} A^{22} & A^{22} A^{12} \\ A^{11} A^{12} & A^{22} A^{12} & \frac{1-\nu}{2} A^{11} A^{22} + \frac{1+\nu}{2} A^{12} A^{12} \end{bmatrix}. \quad (21)$$

2.3. Equilibrium equations

The total potential energy functional of the shell is

$$\Pi(\mathbf{U}) = \int_M ({}_0W(\epsilon_{\alpha\beta}(\mathbf{U})) + {}_1W(\kappa_{\alpha\beta}(\mathbf{U}))) dA - \int_M \mathbf{U} \cdot \mathbf{p} dA + \int_M \frac{1}{2} K_s (U_3)^2 dA, \quad (22)$$

where ${}_0W$ and ${}_1W$ are the membrane and the bending strain energy functions, respectively, \mathbf{p} is the surface loading, and $U_3 = \mathbf{U} \cdot \mathbf{A}_3$ is normal displacement. With K_s we denote the stiffness of the elastic foundation, as in [25] and [26]. Of course, the boundary loading may also exist, and in this case the boundary integral has to be added to (22).

The mechanical system is in equilibrium, when the potential energy functional is at its minimum. The necessary condition is

$$\delta \Pi = \frac{d}{d\epsilon} [\Pi(\mathbf{U} + \epsilon \delta \mathbf{U})] \Big|_{\epsilon=0} = 0, \quad (23)$$

where $\delta \Pi$ denotes the variation of the potential energy, and ϵ is a scalar parameter. By inserting Eq. (22) into Eq. (23) we get

$$\delta \Pi(\mathbf{U}, \delta \mathbf{U}) = \int_M (\delta \epsilon_{\alpha\beta} N^{\alpha\beta} + \delta \kappa_{\alpha\beta} M^{\alpha\beta}) dA - \int_M \delta \mathbf{U} \cdot \mathbf{p} dA + \int_M \delta U_3 K_s U_3 dA = 0, \quad (24)$$

where $\delta \mathbf{U}$ and δU_3 are kinematically admissible variations of displacement field from (8) and normal displacement field, and $\delta \epsilon_{\alpha\beta}, \delta \kappa_{\alpha\beta}$ are variations of membrane and bending strains, respectively.

3. Edge curves for quadrilateral finite element

Let us construct the boundary of a discrete-Kirchhoff–Love shell finite element, which has four nodes and four edge curves spanning between the nodes. The spatial locations of the nodes and the unit normal vectors to the shell mid-surface at the nodes are given. This implies that the tangent planes to the shell mid-surface at the nodes are known as well. The construction of the edge curves will be presented only for the initial configuration, because exactly the same procedure is also valid for the deformed configuration. Let us note that the capital Latin letter index from the index set $\{1, 2, 3, 4\}$ (usually on the left hand side of a particular symbol) stands for the finite element node.

3.1. Edge curves

Following Refs. [27] and [28], we choose the functional, which can be associated with the bending of a spatial curve $\mathbf{R}(t)$,

$$I(\mathbf{R}) = \int_{t_0}^{t_1} \mathbf{R}''(t) \cdot \mathbf{R}''(t) dt. \quad (25)$$

Here, t is a curvilinear coordinate that has values t_0 and t_1 at the start and end nodes, respectively. We search for the optimal equation

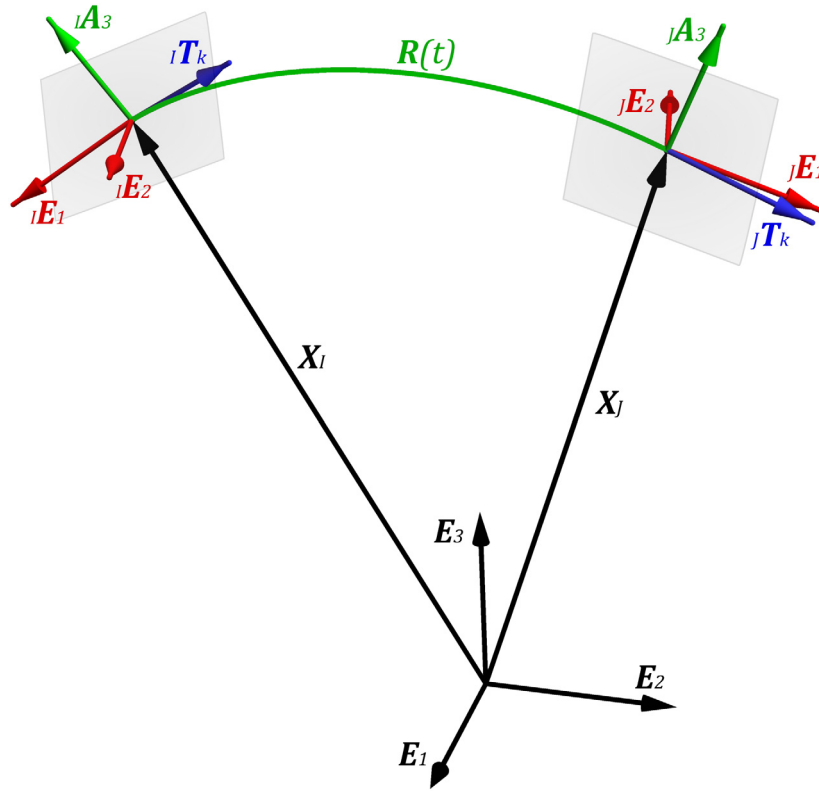


Fig. 1. Edge curve with the tangent vector, tangent plane, and orthonormal basis at its start and end point.

of function $R(t)$ by using the calculus of variations as described in Appendix, see Eqs. (99)–(115). The solution

$$R(t) = t^3 C_4 + t^2 C_3 + t C_2 + C_1, \quad (26)$$

where C_I are constant vectors, gives the edge curve with the least bending. Two boundary conditions for defining C_I are the spatial locations of the start and end node. The remaining two boundary conditions are the tangent vectors to the curve at the start and end node, which are required to be on the corresponding mid-surface tangent planes.

For the edge curve spanning between nodes I and J of the finite element, the boundary conditions are:

$$R(t_0) = X_I, \quad R(t_1) = X_J, \quad R'(t_0) = {}_I T_k, \quad R'(t_1) = {}_J T_k, \quad (27)$$

where X_I and ${}_I T_k$ are the position vector and the tangent vector for node I , respectively, and $k \in \{1, 2\}$ reflects that there are two edge curves at node I , each of them having its own tangent vector. By inserting (27) into (26), we get:

$$R(t) = X_I \frac{(t-t_1)^2(2t-3t_0+t_1)}{(-t_0+t_1)^3} + X_J \frac{(t-t_0)^2(2t+t_0-3t_1)}{(t_0-t_1)^3} + {}_I T_k \frac{(t-t_0)(t-t_1)^2}{(t_0-t_1)^2} + {}_J T_k \frac{(t-t_0)^2(t-t_1)}{(t_0-t_1)^2}. \quad (28)$$

If Eq. (28) is to cover all four edges of the finite element, the indices in Eq. (28) should be used in the following order (see Fig. 5)

$$I = \{1, 2, 4, 1\}, \quad J = \{2, 3, 3, 4\}, \quad k = \{1, 2, 1, 2\}. \quad (29)$$

Moreover, the curvilinear coordinate t should be associated with the isoparametric coordinates of the finite element, $\xi^1 \in [-1, 1]$ and $\xi^2 \in [-1, 1]$, which approximate the curvilinear coordinates over the shell mid-surface from Section 2. In Eq. (28), the following order should be used

$$t = \{\xi^1, \xi^2, \xi^1, \xi^2\} \quad (30)$$

to be in accordance with Eq. (29).

For a particular edge curve between nodes $I = 1$ and $J = 2$, we have

$$t = \xi^1, \quad R(\xi^1) = X(\xi^1, -1), \quad t_0 = -1, \quad t_1 = 1, \quad k = 1, \quad (31)$$

and the boundary conditions (27) are specified as

$$X_I = X_1, \quad X_J = X_2, \quad {}_I T_k = {}_1 A_1, \quad {}_J T_k = {}_2 A_1, \quad (32)$$

which reminds us that the nodal tangent vector equals the nodal covariant basis vector. The following notation is used: ${}_I A_\alpha$ is the covariant basis vector A_α , see Eq. (2), at the finite element node I . Consequently, the relations for the edge curve between nodes $I = 4$ and $J = 3$ are

$${}_I T_k = {}_4 A_1, \quad {}_J T_k = {}_3 A_1, \quad (33)$$

and for the curves between nodes $I = 2$ and $J = 3$, and $I = 1$ and $J = 4$,

$${}_I T_k = {}_2 A_2, \quad {}_J T_k = {}_3 A_2, \quad \text{and} \quad {}_I T_k = {}_1 A_2, \quad {}_J T_k = {}_4 A_2, \quad (34)$$

respectively.

3.2. Nodal tangent vectors of the edge curves

Let us create an orthonormal vector basis at each node of the finite element. The third vector of such a basis at node I is given by a unit normal vector ${}_I A_3$. The other two vectors, ${}_I E_1$ and ${}_I E_2$, are perpendicular to it and to each other, but otherwise arbitrary, see Fig. 1. With the nodal orthonormal bases at hand, the tangent vectors for the edge curve between nodes I and J can be expressed by the following linear combinations:

$${}_I T_k = {}_I \alpha_1^k {}_I E_1 + {}_I \alpha_2^k {}_I E_2, \quad (35)$$

$${}_J T_k = {}_J \alpha_1^k {}_J E_1 + {}_J \alpha_2^k {}_J E_2. \quad (36)$$

In order to define ${}_I\alpha_1^k, {}_I\alpha_2^k, {}_J\alpha_1^k$ and ${}_J\alpha_2^k$, we insert Eqs. (35) and (36) into (28). Moreover, we plug the resulting expression into (25) to get the bending deformation energy of the edge curve, Eq. (25), as a function of four unknowns:

$$\begin{aligned} I({}_I\alpha_1^k, {}_I\alpha_2^k, {}_J\alpha_1^k, {}_J\alpha_2^k) = & -\frac{4}{(t_0 - t_1)^3} \\ & \times \left((t_0 - t_1)^2 ({}_I\alpha_1^k)^2 + (t_0 - t_1) {}_I\alpha_1^k {}_I\alpha_2^k {}_I\mathbf{E}_1 \cdot {}_J\mathbf{E}_1 + \right. \\ & (t_0 - t_1) \left((t_0 - t_1) {}_I\alpha_1^k {}_I\alpha_2^k {}_I\mathbf{E}_1 \cdot {}_J\mathbf{E}_2 - 3 {}_I\alpha_1^k {}_I\alpha_2^k {}_I\mathbf{E}_1 \cdot \mathbf{X}_I + \right. \\ & 3 {}_I\alpha_1^k {}_I\alpha_2^k {}_I\mathbf{E}_1 \cdot \mathbf{X}_J + t_0 ({}_I\alpha_1^k)^2 - t_1 ({}_I\alpha_2^k)^2 + t_0 {}_I\alpha_1^k {}_I\alpha_2^k {}_I\mathbf{E}_1 \cdot {}_J\mathbf{E}_2 - \\ & t_1 {}_I\alpha_1^k {}_I\alpha_2^k {}_I\mathbf{E}_1 \cdot {}_J\mathbf{E}_2 - 3 {}_I\alpha_1^k {}_I\alpha_2^k {}_I\mathbf{E}_1 \cdot \mathbf{X}_I \\ & + 3 {}_I\alpha_1^k {}_I\alpha_2^k {}_I\mathbf{E}_1 \cdot \mathbf{X}_J + t_0 ({}_I\alpha_2^k)^2 - \\ & t_1 ({}_I\alpha_1^k)^2 + t_0 {}_I\alpha_2^k {}_I\alpha_1^k {}_I\mathbf{E}_2 \cdot {}_J\mathbf{E}_2 - t_1 {}_I\alpha_2^k {}_I\alpha_1^k {}_I\mathbf{E}_2 \cdot {}_J\mathbf{E}_2 \\ & - 3 {}_I\alpha_2^k {}_I\alpha_1^k {}_I\mathbf{E}_2 \cdot \mathbf{X}_I + \\ & 3 {}_I\alpha_2^k {}_I\alpha_1^k {}_I\mathbf{E}_2 \cdot \mathbf{X}_J + t_0 ({}_I\alpha_2^k)^2 - t_1 ({}_I\alpha_1^k)^2 - 3 {}_I\alpha_2^k {}_I\alpha_1^k {}_I\mathbf{E}_2 \cdot \mathbf{X}_I \\ & \left. + 3 {}_I\alpha_2^k {}_I\alpha_1^k {}_I\mathbf{E}_2 \cdot \mathbf{X}_J \right) + \\ & 3 ({}_I\mathbf{X}_I \cdot \mathbf{X}_I - 2 {}_I\mathbf{X}_I \cdot \mathbf{X}_J + {}_I\mathbf{X}_J \cdot \mathbf{X}_J). \end{aligned} \quad (37)$$

We search for α -s that minimize (37) and provide edge curve with the least bending. For this purpose, the following four equations are formed

$$\frac{\partial I({}_I\alpha_1^k, {}_I\alpha_2^k, {}_J\alpha_1^k, {}_J\alpha_2^k)}{\partial \chi^k \alpha_\omega} = 0, \quad \chi \in \{I, J\}, \quad \omega \in \{1, 2\}. \quad (38)$$

The solution of this linear system is given in (116)–(119) in Appendix. With known α -s, the nodal tangent vectors to the edge curves can be written node-by-node as:

$${}_1\mathbf{A}_1 = {}_1\alpha_1^1 {}_1\mathbf{E}_1 + {}_1\alpha_2^1 {}_1\mathbf{E}_2, \quad {}_1\mathbf{A}_2 = {}_1\alpha_1^2 {}_1\mathbf{E}_1 + {}_1\alpha_2^2 {}_1\mathbf{E}_2, \quad (39)$$

$${}_2\mathbf{A}_1 = {}_2\alpha_1^1 {}_2\mathbf{E}_1 + {}_2\alpha_2^1 {}_2\mathbf{E}_2, \quad {}_2\mathbf{A}_2 = {}_2\alpha_1^2 {}_2\mathbf{E}_1 + {}_2\alpha_2^2 {}_2\mathbf{E}_2, \quad (40)$$

$${}_3\mathbf{A}_1 = {}_3\alpha_1^1 {}_3\mathbf{E}_1 + {}_3\alpha_2^1 {}_3\mathbf{E}_2, \quad {}_3\mathbf{A}_2 = {}_3\alpha_1^2 {}_3\mathbf{E}_1 + {}_3\alpha_2^2 {}_3\mathbf{E}_2, \quad (41)$$

$${}_4\mathbf{A}_1 = {}_4\alpha_1^1 {}_4\mathbf{E}_1 + {}_4\alpha_2^1 {}_4\mathbf{E}_2, \quad {}_4\mathbf{A}_2 = {}_4\alpha_1^2 {}_4\mathbf{E}_1 + {}_4\alpha_2^2 {}_4\mathbf{E}_2, \quad (42)$$

and applied as boundary conditions, see (32)–(34), to obtain the edge curves with G^1 continuity at nodes.

3.3. Continuity between the elements

For a set of elements, attached to a given node of the mesh, the edge curves that meet at that node have their tangent vectors on the unique tangent plane to the shell mid-surface. That makes the approximated shell mid-surface G^1 -continuous across the nodes of the mesh. However, the continuity along the edge of the element, in the direction perpendicular to the edge is only C^0 , as two elements with the same edge do not necessarily share the same tangent plane at all points of this edge. Fig. 2 shows a schematic presentation of the continuity between a patch of finite elements.

To conclude Section 3, we note once again that exactly the same procedure must be repeated to construct the edge curves in the deformed configuration by using the orthonormal coordinate system, denoted as $\{{}_I\mathbf{e}_1, {}_I\mathbf{e}_2, {}_I\mathbf{a}_3\}$ for node I , see Fig. 3, that is completely defined by nodal rotations as shown in Section 4.3.

4. Coons patch between the edge curves

In this section, we span the bilinear Coons patch between the above defined Hermite edge curves. To this end, we use the following notation: $\mathbf{X}(\xi^1, -1)$, $\mathbf{X}(\xi^1, 1)$, $\mathbf{X}(-1, \xi^2)$ and $\mathbf{X}(1, \xi^2)$ for the edge curves from the initial configuration, which are defined between nodes 1 and 2, 4 and 3, 1 and 4, and 2 and 3, respectively, by Eq. (28).

4.1. Bilinear Coons patch

Three surfaces are combined in order to form the Coons patch between the edge curves. The first surface spans between $\mathbf{X}(\xi^1, -1)$ and $\mathbf{X}(\xi^1, 1)$ as

$$\mathbf{X}_c(\xi^1, \xi^2) = \left(1 - \frac{\xi^2 - \xi_0^2}{\xi_1^2 - \xi_0^2}\right) \mathbf{X}(\xi^1, -1) + \left(\frac{\xi^2 - \xi_0^2}{\xi_1^2 - \xi_0^2}\right) \mathbf{X}(\xi^1, 1), \quad (43)$$

the second surface is defined between $\mathbf{X}(-1, \xi^2)$ and $\mathbf{X}(1, \xi^2)$ as

$$\mathbf{X}_d(\xi^1, \xi^2) = \left(1 - \frac{\xi^1 - \xi_0^1}{\xi_1^1 - \xi_0^1}\right) \mathbf{X}(-1, \xi^2) + \left(\frac{\xi^1 - \xi_0^1}{\xi_1^1 - \xi_0^1}\right) \mathbf{X}(1, \xi^2), \quad (44)$$

whereas the third surface is interpolated only between the nodes, $\mathbf{X}_1 = \mathbf{X}(-1, -1)$, $\mathbf{X}_2 = \mathbf{X}(1, -1)$, $\mathbf{X}_3 = \mathbf{X}(1, 1)$ and $\mathbf{X}_4 = \mathbf{X}(-1, 1)$, as

$$\begin{aligned} \mathbf{X}_{cd}(\xi^1, \xi^2) = & \left[\left(1 - \frac{\xi^1 - \xi_0^1}{\xi_1^1 - \xi_0^1}\right) \quad \left(\frac{\xi^1 - \xi_0^1}{\xi_1^1 - \xi_0^1}\right) \right] \begin{bmatrix} \mathbf{X}(-1, -1) & \mathbf{X}(-1, 1) \\ \mathbf{X}(1, -1) & \mathbf{X}(1, 1) \end{bmatrix} \\ & \times \begin{bmatrix} \left(1 - \frac{\xi^2 - \xi_0^2}{\xi_1^2 - \xi_0^2}\right) \\ \left(\frac{\xi^2 - \xi_0^2}{\xi_1^2 - \xi_0^2}\right) \end{bmatrix}. \end{aligned} \quad (45)$$

The following combination, see Fig. 4, defines the bilinear Coons patch between the four Hermite edge curves:

$$\mathbf{X}(\xi^1, \xi^2) = \mathbf{X}_c(\xi^1, \xi^2) + \mathbf{X}_d(\xi^1, \xi^2) - \mathbf{X}_{cd}(\xi^1, \xi^2). \quad (46)$$

The constants in Eqs. (43)–(45) are

$$\xi_0^1 = -1, \quad \xi_1^1 = 1, \quad \xi_0^2 = -1, \quad \xi_1^2 = 1. \quad (47)$$

4.2. Finite element interpolations

Eq. (46) can be rewritten in a more standard way, by presenting the initial surface of the finite element in terms of nodal values

$$\mathbf{X}(\xi^1, \xi^2) = \sum_{I=1}^4 ({}_I N_I \mathbf{X}_I + {}_I N_2 {}_I \mathbf{A}_1 + {}_I N_3 {}_I \mathbf{A}_2), \quad (48)$$

where \mathbf{X}_I is the location of the node, and ${}_I \mathbf{A}_1$ and ${}_I \mathbf{A}_2$ are nodal covariant tangent basis vectors, defined in Section 3.2. The deformed surface of the finite element is interpolated in the same way as

$$\mathbf{x}(\xi^1, \xi^2) = \sum_{I=1}^4 ({}_I N_I \mathbf{x}_I + {}_I N_2 {}_I \mathbf{a}_1 + {}_I N_3 {}_I \mathbf{a}_2), \quad (49)$$

where \mathbf{x}_I is the location of the node, and ${}_I \mathbf{a}_1$ and ${}_I \mathbf{a}_2$ are nodal covariant basis vectors, all in deformed configuration. The difference between Eqs. (49) and (48) yields displacements of the surface of the element as:

$$\mathbf{U}(\xi^1, \xi^2) = \sum_{I=1}^4 ({}_I N_I {}_I \mathbf{u} + {}_I N_2 ({}_I \mathbf{a}_1 - {}_I \mathbf{A}_1) + {}_I N_3 ({}_I \mathbf{a}_2 - {}_I \mathbf{A}_2)), \quad (50)$$

where ${}_I \mathbf{u}$ is nodal displacement.

Here, ${}_I N_1$, ${}_I N_2$ and ${}_I N_3$ are interpolation functions of the third order, see Appendix, Eqs. (121)–(123), that yield from using the Hermite edge curves and the bilinear Coons patch. These interpolation functions characterize the derived finite element, because (48) and (49) are applied to compute the (real and virtual) curvatures and membrane strains, and consequently moments and membrane forces, in a way presented in Section 2.

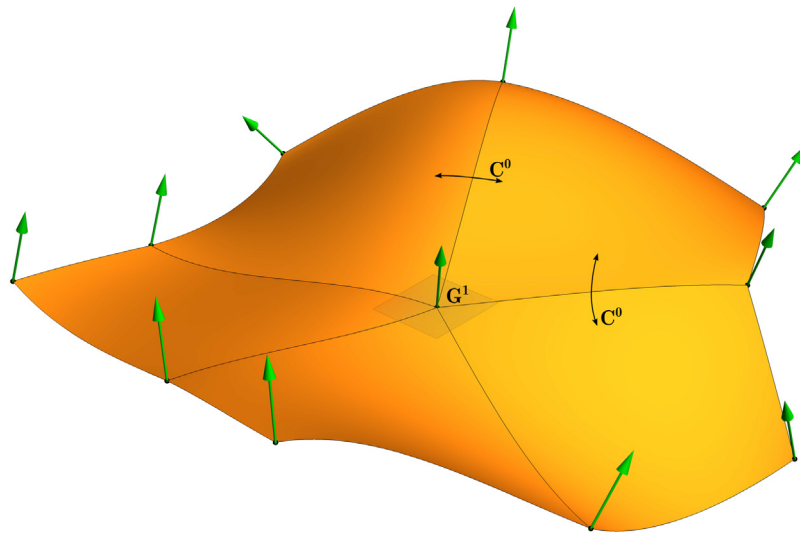


Fig. 2. Illustration of continuity between the set of elements attached to a given node.

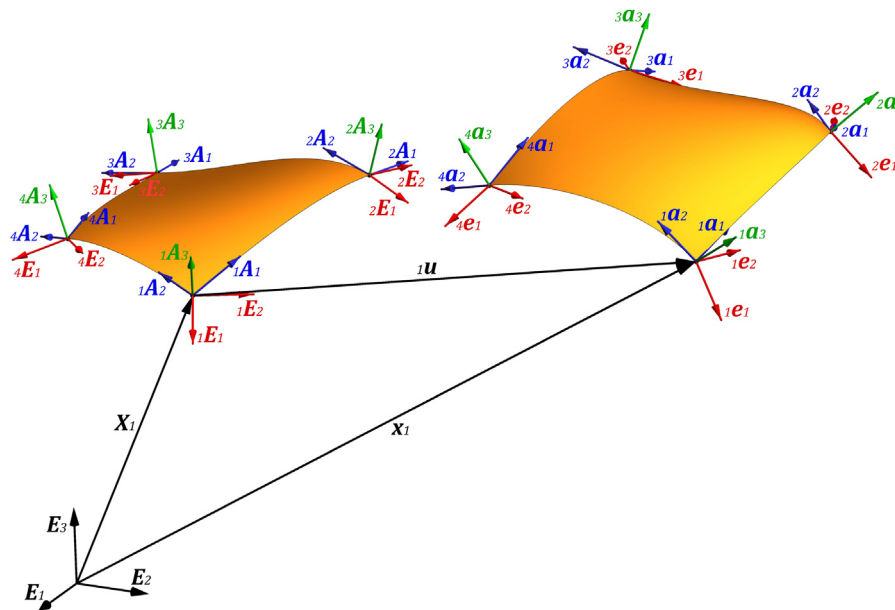


Fig. 3. Initial (left) and deformed (right) configuration of the finite element, with nodal orthonormal bases and nodal covariant base vectors.

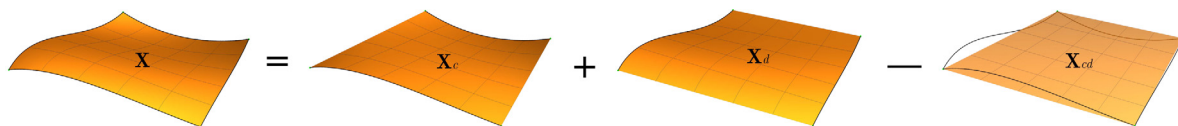


Fig. 4. Schematic representation of X_c , X_d and X_{cd} surfaces assembled into the bilinear Coons patch X .

4.3. Nodal values in current configuration

Eq. (49) shows that the deformed surface of the finite element is completely defined by the position of the nodes and by the nodal covariant basis vectors. The position of the node is given simply as

$${}_I \mathbf{x} = {}_I \mathbf{X} + {}_I \mathbf{u}. \tag{51}$$

Computing the nodal covariant basis vectors at the deformed configuration is more demanding. One must first determine the nodal orthonormal basis vectors ${}_I e_\alpha, {}_I a_3$ by rotating the corresponding orthonormal basis ${}_I E_\alpha, {}_I A_3$ from the initial configuration, e.g. [29]. In

this respect, we can represent the initial nodal normal vector as

$${}_I \mathbf{A}_3 = {}_I \mathbf{A}_0 E_3, \tag{52}$$

where $E_3 = [0, 0, 1]^T$ is the third basis vector of the fixed orthonormal basis in the 3D space, into which the discretized shell mid-surface is embedded, see Figs. 1 and 3. Here, ${}_I \mathbf{A}_0$ is the initial nodal rotation matrix, given simply as

$${}_I \mathbf{A}_0 = [{}_I E_1, {}_I E_2, {}_I A_3]. \tag{53}$$

With ${}_I A_0$ at hand, the nodal normal vector in the deformed configuration can be obtained by a composition of two rotations as

$${}_I a_3 = {}_I A_0 {}_I \tilde{\Lambda}({}_I \vartheta) E_3, \quad (54)$$

where ${}_I \vartheta$ collects the material parameters that parametrize the second rotation. In this work, we apply the (pseudo) rotation vector for ${}_I \vartheta$, making use of the Rodrigues formula to represent the second rotation, e.g. [2,29–31]

$${}_I \tilde{\Lambda}({}_I \vartheta) = \cos({}_I \vartheta) \mathbf{I} + \frac{\sin({}_I \vartheta)}{{}_I \vartheta} {}_I \hat{\vartheta} + \frac{1 - \cos({}_I \vartheta)}{({}_I \vartheta)^2} {}_I \vartheta \otimes {}_I \vartheta. \quad (55)$$

Here, ${}_I \hat{\vartheta}$ is a skew-symmetric matrix, thus ${}_I \hat{\vartheta} b = {}_I \vartheta \times b$ for any $b \in \mathbb{R}^3$ and ${}_I \vartheta = \|{}_I \vartheta\|$. With the above definition for ${}_I \tilde{\Lambda}({}_I \vartheta)$, the drilling rotation is excluded, making ${}_I \vartheta$ a vector with only two non zero components. Taking this into account, a simplification of Eq. (54) is obtained:

$${}_I a_3 = {}_I A_0 {}_I \tilde{\Lambda}({}_I \vartheta) E_3 = {}_I A_0 \left[\cos({}_I \vartheta) E_3 + \frac{\sin({}_I \vartheta)}{{}_I \vartheta} {}_I \vartheta \times E_3 \right]. \quad (56)$$

In the same way, the remaining two vectors of the nodal orthonormal basis in the deformed configuration are obtained as

$${}_I e_1 = {}_I A_0 {}_I \tilde{\Lambda}({}_I \vartheta) E_1 = {}_I A_0 \left[\cos({}_I \vartheta) E_1 + \frac{\sin({}_I \vartheta)}{{}_I \vartheta} {}_I \vartheta \times E_1 + \frac{1 - \cos({}_I \vartheta)}{({}_I \vartheta)^2} {}_I \vartheta ({}_I \vartheta \cdot E_1) \right], \quad (57)$$

$${}_I e_2 = {}_I A_0 {}_I \tilde{\Lambda}({}_I \vartheta) E_2 = {}_I A_0 \left[\cos({}_I \vartheta) E_2 + \frac{\sin({}_I \vartheta)}{{}_I \vartheta} {}_I \vartheta \times E_2 + \frac{1 - \cos({}_I \vartheta)}{({}_I \vartheta)^2} {}_I \vartheta ({}_I \vartheta \cdot E_2) \right], \quad (58)$$

where $E_1 = [1, 0, 0]^T$ and $E_2 = [0, 1, 0]^T$.

With the nodal orthonormal basis ${}_I e_\alpha, {}_I a_3$ at hand, the corresponding version of Eqs. (39)–(42) is employed

$${}_1 a_1 = {}_1 \alpha_1 {}_1 e_1 + {}_1 \alpha_2 {}_1 e_2, \quad {}_1 a_2 = {}_2 \alpha_1 {}_1 e_1 + {}_2 \alpha_2 {}_1 e_2, \quad (59)$$

$${}_2 a_1 = {}_2 \alpha_1 {}_2 e_1 + {}_2 \alpha_2 {}_2 e_2, \quad {}_2 a_2 = {}_2 \alpha_1 {}_2 e_1 + {}_2 \alpha_2 {}_2 e_2, \quad (60)$$

$${}_3 a_1 = {}_3 \alpha_1 {}_3 e_1 + {}_3 \alpha_2 {}_3 e_2, \quad {}_3 a_2 = {}_3 \alpha_1 {}_3 e_1 + {}_3 \alpha_2 {}_3 e_2, \quad (61)$$

$${}_4 a_1 = {}_4 \alpha_1 {}_4 e_1 + {}_4 \alpha_2 {}_4 e_2, \quad {}_4 a_2 = {}_4 \alpha_1 {}_4 e_1 + {}_4 \alpha_2 {}_4 e_2, \quad (62)$$

to get the nodal covariant basis vectors in the deformed configuration. To get 16 scalar parameters from Eqs. (59)–(62), the corresponding versions of Eqs. (116)–(119) in Appendix are applied with $x_I, x_J, {}_I e_1, {}_I e_2, {}_J e_1, {}_J e_2$ replacing $X_I, X_J, {}_I E_1, {}_I E_2, {}_J E_1, {}_J E_2$.

We note that by applying the finite rotation description (56)–(58) in (23), an additive update of the (pseudo) rotation vector at the node of the element is performed. The theoretical background for this kind of rotational update is explained in e.g. [30,31], and the practical implementation with illustrative numerical examples is presented in e.g. [2,29].

5. Assumed natural strains and variational formulation

5.1. ANS concept for membrane strains

The following ANS interpolation was suggested in [32] for curing the membrane locking for the four-node shell element

$$\begin{aligned} \epsilon_{11} &= \frac{1}{2}(1 - \xi^2)\epsilon_{11}(A) + \frac{1}{2}(1 + \xi^2)\epsilon_{11}(C), \\ \epsilon_{22} &= \frac{1}{2}(1 - \xi^1)\epsilon_{22}(D) + \frac{1}{2}(1 + \xi^1)\epsilon_{22}(B), \end{aligned} \quad (63)$$

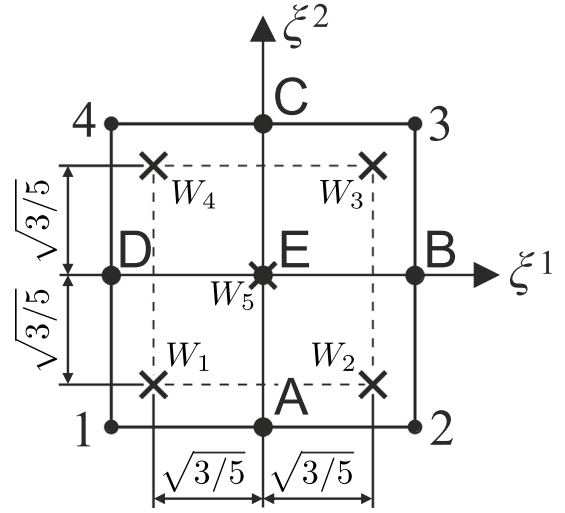


Fig. 5. Tying points for ANS membrane strain interpolation scheme. Gauss points for 5-point quadrature rule with $W_1 = W_2 = W_3 = W_4 = 5/9$ and $W_5 = 16/9$ weights.

$$\epsilon_{12} = \epsilon_{12}(E),$$

where, $\epsilon_{11}(A), \epsilon_{11}(C), \epsilon_{22}(D), \epsilon_{22}(B)$ and $\epsilon_{12}(E)$ are the strains evaluated at the points shown in Fig. 5. However, with the ANS from Eq. (63), the shell element does not pass the membrane patch test. This deficiency can be removed, see [3], by using a higher-order assumed strain interpolation

$$\begin{aligned} \epsilon_{11} &= \epsilon_{11}^{00} + \xi^2 \epsilon_{11}^{01} + (\xi^2)^2 \epsilon_{11}^{02}, \\ \epsilon_{22} &= \epsilon_{22}^{00} + \xi^1 \epsilon_{22}^{10} + (\xi^1)^2 \epsilon_{22}^{20}, \\ \epsilon_{12} &= \epsilon_{12}^{00} + \xi^1 \epsilon_{12}^{10} + \xi^2 \epsilon_{12}^{01} + \xi^1 \xi^2 \epsilon_{12}^{11}, \end{aligned} \quad (64)$$

and calibrating the coefficients so that Eqs. (64) satisfy the compatibility equation for the plane membrane problem

$$\frac{\partial^2 \epsilon_{11}}{\partial \xi^2 \partial \xi^2} - 2 \frac{\partial^2 \epsilon_{12}}{\partial \xi^1 \partial \xi^2} + \frac{\partial^2 \epsilon_{22}}{\partial \xi^1 \partial \xi^1} = 2\Gamma_{12}^1 \frac{\partial \epsilon_{11}}{\partial \xi^2} + 2\Gamma_{12}^2 \frac{\partial \epsilon_{22}}{\partial \xi^1} - 2\Gamma_{12}^\alpha \Gamma_{12}^\beta \epsilon_{\alpha\beta}. \quad (65)$$

Here, Γ_{12}^1 and Γ_{12}^2 are Christoffel's symbols, defined in Eq. (15).

Our implementation of ANS follows [3], except for the choice of the plane to deal with the plane membrane problem. We use the plane defined by the following two vectors

$$t_1 = \frac{d_1 + d_2}{\|d_1 + d_2\|}, \quad t_2 = \frac{d_1 - d_2}{\|d_1 - d_2\|}, \quad (66)$$

where

$$d_1 = \frac{X_3 - X_1}{\|X_3 - X_1\|}, \quad d_2 = \frac{X_2 - X_4}{\|X_2 - X_4\|}. \quad (67)$$

The properties of the projection of the shell mid-surface on that plane are illustrated in [5]. The determinant of the transformation (i.e. the Jacobian) matrix between the coordinates in the plane defined by t_α and the curvilinear coordinates ξ^α can be given simply as

$$A = c_0 + c_\alpha \xi^\alpha, \quad (68)$$

where c_0 and c_α are constants. Because the covariant base vectors in the plane are

$$A_1 = A_1^0 + \xi^2 \bar{A}, \quad A_2 = A_2^0 + \xi^1 \bar{A}, \quad (69)$$

$$A_1^0 = \sum_{I=1}^4 a_{1I} {}_I X, \quad A_2^0 = \sum_{I=1}^4 a_{2I} {}_I X, \quad \bar{A} = \sum_{I=1}^4 h_I {}_I X, \quad (70)$$

where $a_{1I} = \frac{1}{4}\xi_I$, $a_{2I} = \frac{1}{4}\eta_I$, $h_I = \frac{1}{4}\xi_I\eta_I$, $\xi_I \in \{-1, 1, 1, -1\}$ and $\eta_I \in \{-1, -1, 1, 1\}$, one has

$$\begin{aligned} c_0 &= (A_1^0 \cdot t_1)(A_2^0 \cdot t_2) - (A_2^0 \cdot t_1)(A_1^0 \cdot t_2), \\ c_1 &= (A_1^0 \cdot t_1)(\bar{A} \cdot t_2) - (\bar{A} \cdot t_1)(A_1^0 \cdot t_2), \\ c_2 &= (\bar{A} \cdot t_1)(A_2^0 \cdot t_2) - (A_2^0 \cdot t_1)(\bar{A} \cdot t_2), \end{aligned} \quad (71)$$

and

$$\Gamma_{12}^1 = \frac{1}{A}c_2, \quad \Gamma_{12}^2 = \frac{1}{A}c_1. \quad (72)$$

After substituting ANS interpolations (64) into the compatibility equation (65), the following relations are obtained

$$\epsilon_{11}^{01} = \epsilon_{22}^{20} = \epsilon_{12}^{11} = \epsilon_*, \quad 2\epsilon_{12}^{10} = \epsilon_{11}^{01}, \quad 2\epsilon_{12}^{01} = \epsilon_{22}^{10}, \quad (73)$$

$$\epsilon_* = \frac{c_2}{c_0}(\epsilon_{11}^{01} - \frac{c_2}{c_0}\epsilon_{11}^{00}) + \frac{c_1}{c_0}(\epsilon_{22}^{10} - \frac{c_1}{c_0}\epsilon_{22}^{00}) - \frac{2c_1c_2}{c_0^2}\epsilon_{12}^{00}. \quad (74)$$

indicating that there are only five independent coefficients in Eq. (64). If we now use 4 tying points A, B, C and D, see Fig. 5, for the in-plane normal strains and one tying point E for the in-plane shear strain, and insert Eqs. (73)–(74) into Eq. (64), we get the following expressions for the ANS strains:

$$\begin{aligned} \epsilon_{11} &= \frac{1}{2}(1 - \xi^2)\epsilon_{11}(A) + \frac{1}{2}(1 + \xi^2)\epsilon_{11}(C) - (1 - (\xi^2)^2)\tilde{\epsilon}_*, \\ \epsilon_{22} &= \frac{1}{2}(1 - \xi^1)\epsilon_{22}(D) + \frac{1}{2}(1 + \xi^1)\epsilon_{22}(B) - (1 - (\xi^1)^2)\tilde{\epsilon}_*, \\ \epsilon_{12} &= \epsilon_{12}(E) + \frac{1}{4}\xi^1(\epsilon_{11}(C) - \epsilon_{11}(A)) + \frac{1}{4}\xi^2(\epsilon_{22}(B) - \epsilon_{22}(D)) + \xi^1\xi^2\tilde{\epsilon}_*, \end{aligned} \quad (75)$$

where

$$\begin{aligned} \tilde{\epsilon}_* &= -\frac{c_2(c_0 + c_2)}{2d}\epsilon_{11}(A) + \frac{c_2(c_0 - c_2)}{2d}\epsilon_{11}(C) - \\ &\frac{c_1(c_0 + c_1)}{2d}\epsilon_{22}(D) + \frac{c_1(c_0 - c_1)}{2d}\epsilon_{22}(B) - \frac{2c_1c_2(c_0 + c_2)}{d}\epsilon_{12}(E) \end{aligned} \quad (76)$$

and

$$d = c_0^2 - c_1^2 - c_2^2. \quad (77)$$

5.2. Potential energy, its variation and linearization

The total potential energy of the derived shell finite element with the Saint-Venant Kirchhoff constitutive relation, elastic foundation and surface loading p can be written as, see (22):

$$\begin{aligned} \Pi^e(U) &= \int_{M^e} \frac{Eh}{2(1-\nu^2)} (\epsilon^{ANS} \cdot \mathbf{H} \epsilon^{ANS} + \frac{h^2}{12} \boldsymbol{\kappa} \cdot \mathbf{H} \boldsymbol{\kappa}) dA^e - \\ &\int_{M^e} \mathbf{U} \cdot \mathbf{p} dA^e + \int_{M^e} \frac{1}{2} K_s (U_3)^2 dA^e. \end{aligned} \quad (78)$$

Here, ϵ^{ANS} and $\boldsymbol{\kappa}$ are vector fields, see Eq. (18), obtained from expressions in Section 2 by using the initial configuration data and \mathbf{U} from (50), which is composed of the mid-surface displacement $\mathbf{u} = \sum_{I=1}^4 N_I \mathbf{u}$ and the rotation-related vector fields that are completely defined by the interpolation functions (121)–(123) and nodal dofs. The ANS subscript in (78) reminds that the membrane strains are computed in accordance with the developments from Section 5.1. Furthermore, \mathbf{H} is from Eq. (21), and M^e denotes the mid-surface of the shell finite element in the undeformed configuration. Numerical tests demonstrated that replacement of \mathbf{U} in the last two integrals in (78) with simpler $\tilde{\mathbf{u}} = \sum_{I=1}^4 \tilde{N}_I(\xi^1, \xi^2) \mathbf{u}$, where \tilde{N}_I are the bilinear Lagrange interpolation functions, yields a negligible difference in results. The variation of the potential energy of the element is

$$\delta \Pi^e = \frac{d}{d\epsilon} [\Pi^e(U + \epsilon \delta U)] \Big|_{\epsilon=0} = 0, \quad (79)$$

where ϵ is a scalar parameter. By applying the formalism (79) in Eq. (78) one gets

$$\delta \Pi^e(U, \delta U) = \int_{M^e} \frac{Eh}{1-\nu^2} (\delta \epsilon^{ANS} \cdot \mathbf{H} \epsilon^{ANS} + \frac{h^2}{12} \delta \boldsymbol{\kappa} \cdot \mathbf{H} \boldsymbol{\kappa}) dA^e$$

$$- \int_{M^e} \delta \mathbf{U} \cdot \mathbf{p} dA^e + \int_{M^e} \delta U_3 K_s U_3 dA^e = 0. \quad (80)$$

The area integrals of the derived element are computed by using the 5 integration point scheme, see e.g. [33], shown in Fig. 5, which for the considered element yields practically the same results as the 3 × 3 Gauss numerical integration rule.

The discretized form of the potential energy (22) and its variation (23) can be written as

$$\Pi = \mathbb{A}_e^{N_{el}} \Pi^e, \quad \delta \Pi = \mathbb{A}_e^{N_{el}} \delta \Pi^e = 0, \quad (81)$$

where \mathbb{A} is the finite element assembly operator and N_{el} is number of elements in the mesh. To solve the resulting system of equilibrium equations by the incremental-iterative Newton–Raphson method, equation (80) must be consistently linearized. We performed the linearization by using Mathematica [34] and its add-on AceGen [35].

6. Numerical examples

The above shell formulation, denoted hereinafter as DKQ-5, was transformed into a computer code using Mathematica's add on AceGen [35], which enables an automatic differentiation of large expressions and algorithms. The computer code for the DKQ-5 was incorporated into the finite element computer program AceFEM [36], which was used to compute the examples presented below. Structured and distorted meshes were used, with mesh distortion described as $r = L_{max}/L_{min}$, where L_{max} and L_{min} are the chosen edge lengths of the largest and smallest finite element in the mesh. For comparison, we also present the results of MITC4 finite element (hereinafter referred to as RM-5), which is the isoparametric, 4-node element, with Reissner–Mindlin kinematics and Bathe–Dvorkin ANS interpolation for the transverse shear strains [37]. Unless stated otherwise, the load control was applied.

6.1. Eigenvalues and eigenmodes

Following [4], we computed eigenvalues of linear stiffness matrix of a single finite element. We choose two geometric configurations, shown in Fig. 6(a) and (b), and the data:

$$a = 2 \text{ mm}, \quad h = 0.02 \text{ mm}, \quad E = 10^8 \text{ MPa}, \quad \nu = 0.3. \quad (82)$$

The first six eigenvalues were zero, indicating that DKQ-5 correctly describes rigid body motions. Fig. 6(a) shows that the DKQ-5 and RM-5 eigenvalues are similar up to the 11th mode and also from the 16th to 20th mode. For lower modes of the distorted element, see Fig. 6(b), the similarity is up to the 10th mode. The eigenmodes for the square DKQ-5 element presented in Fig. 7 indicate that the modes 7–15 are bending modes and the modes 16–20 are membrane modes. For comparison, eigenmode 13 is also represented in bilinear representation (see 13* in Fig. 7). Due to the use of higher order interpolation, the bending eigenmodes of DKQ-5 are much more complex than those of RM-5. DKQ-5 has more bending modes than RM-5, because the latter element also has some transverse shear modes between its bending and membrane modes. This is the reason why the RM-5 curve in Fig. 6(a) and (b) has a jump before the DKQ-5 curve.

In Fig. 6(c) and (d), we show eigenvalues of the linear stiffness matrix obtained for mesh of 10 × 10 flat square elements. The displacements are restricted at two opposite edges of the mesh with the following properties:

$$w = 20 \text{ mm}, \quad h = \{0.02 \text{ for case c), } 0.002 \text{ for case d)\} \text{ mm}, \quad (83)$$

$$E = 10^3 \text{ MPa}, \quad \nu = 0.3.$$

The shapes of the curves are similar to those for single elements.

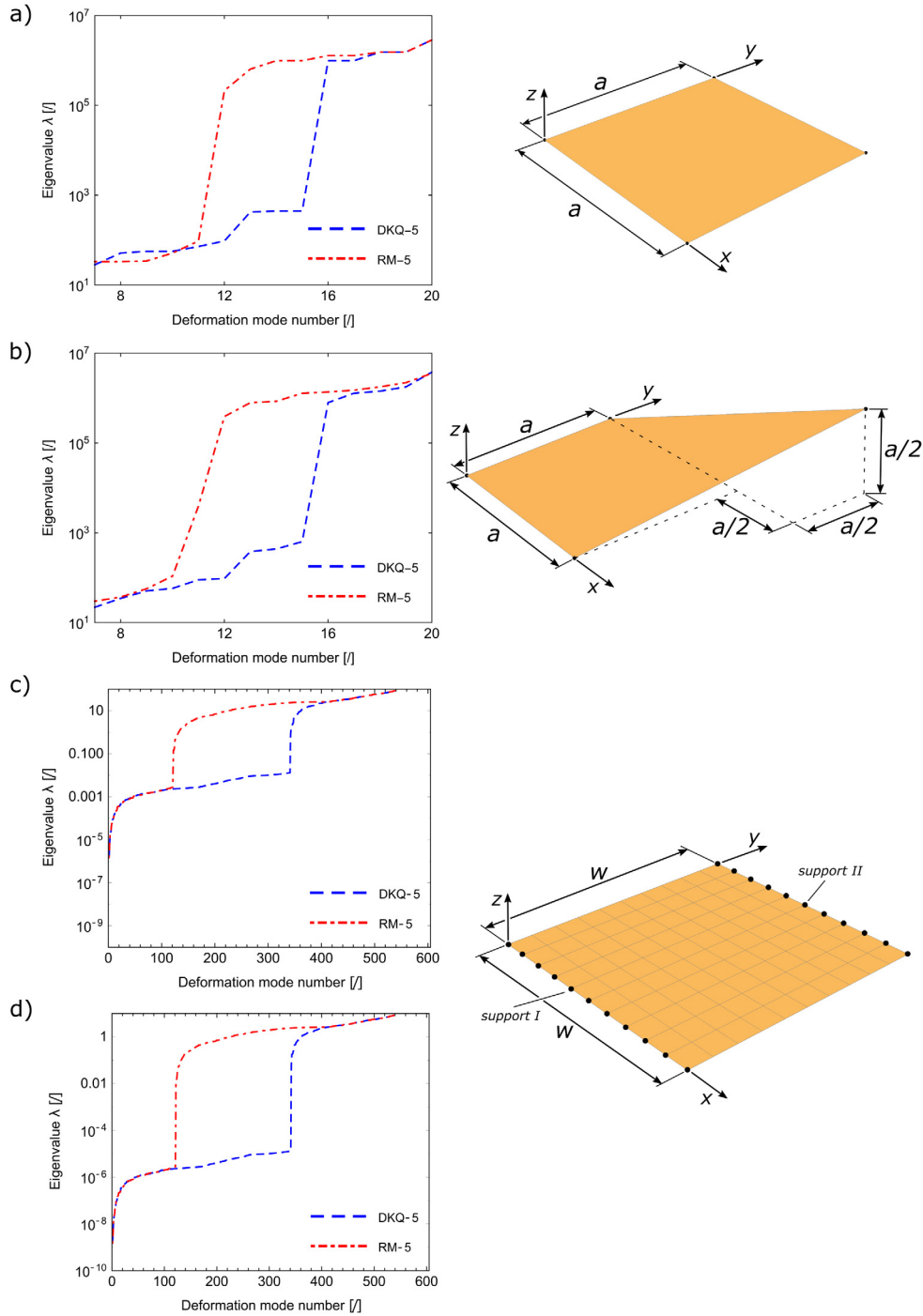


Fig. 6. Linear stiffness matrix eigenvalues for: (a) flat square element, (b) distorted element, (c) and (d) mesh of 10×10 elements, simply supported at two opposite edges.

6.2. Patch tests

The mesh in Fig. 8 is used for the membrane patch test, with the positions of the interior nodes given as $N_5 = \{0.039, 0.021, 0\}$, $N_6 = \{0.18, 0.03, 0\}$, $N_7 = \{0.159, 0.081, 0\}$ and $N_8 = \{0.081, 0.081, 0\}$ mm. The following boundary displacements are set to zero: at node 2 in the x and z -directions, at node 3 in all three directions, and at node 4 in the y and z -directions. At nodes 1 and 4, forces are applied. The rest of the data are:

$$L = 0.24 \text{ mm}, \quad w = 0.12 \text{ mm}, \quad h = 0.001 \text{ mm}, \quad (84)$$

$$E = 1 \cdot 10^6 \text{ MPa}, \quad \nu = 0.25, \quad F_x = -1.2 \text{ N}.$$

The analytical solution for the strains

$$\epsilon_{11} = 2 \cdot 10^{-2}, \quad \epsilon_{22} = -5 \cdot 10^{-3}, \quad \epsilon_{12} = 0, \quad (85)$$

and displacements at nodes 1, 2 and 4

$${}_1\mathbf{u} = \{-4.8 \cdot 10^{-3}, 6 \cdot 10^{-4}, 0\} \text{ mm}, \quad {}_2\mathbf{u} = \{0, 6 \cdot 10^{-4}, 0\} \text{ mm}, \quad (86)$$

$${}_4\mathbf{u} = \{-4.8 \cdot 10^{-3}, 0, 0\} \text{ mm}$$

are matched exactly by DKQ-5 (at the integration points and nodes, respectively).

The same mesh and material properties are assumed for another membrane patch test, see Fig. 9, where displacement control is used. The displacements and rotations are set to zero at node 1. At nodes 2,

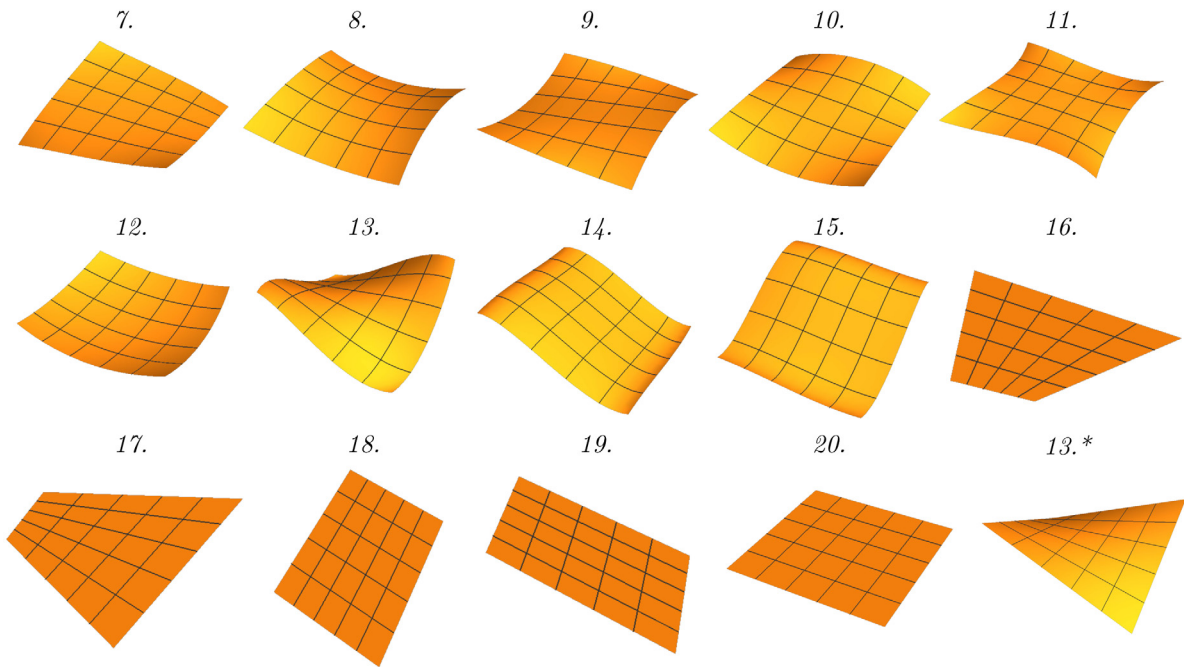


Fig. 7. Eigenmodes of DKQ-5 finite element, case (a) in Fig. 6. Eigenmode 13.* is bilinear representation of eigenmode 13.

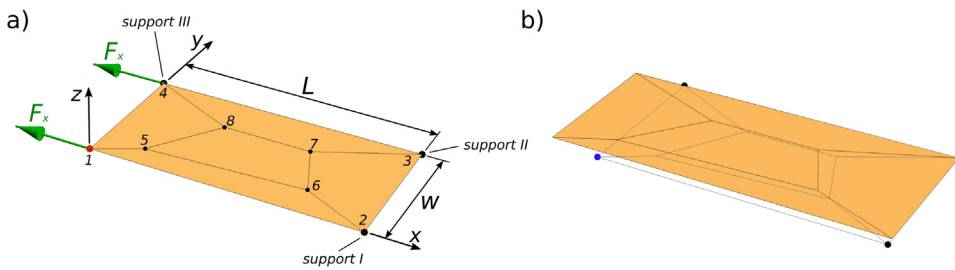


Fig. 8. Membrane patch test with imposed forces: (a) undeformed and (b) deformed configuration (scaling factor is 10).

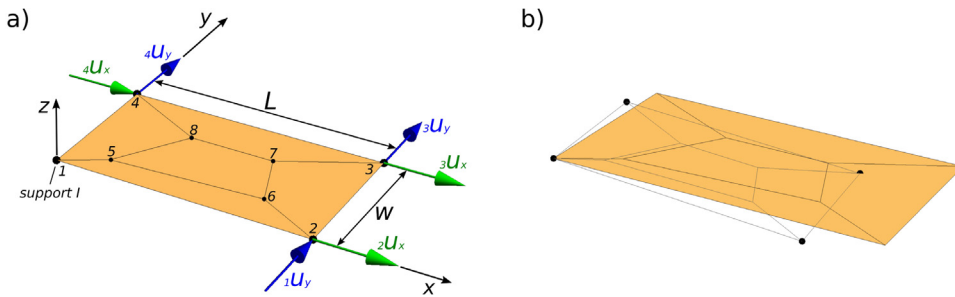


Fig. 9. Membrane patch test with imposed displacements: (a) undeformed and (b) deformed configuration (scaling factor is 250).

3 and 4, the displacements are imposed as:

$${}_2\mathbf{u} = \left\{ L, \frac{L}{2}, 0 \right\} \cdot 10^{-3} \text{ mm}, \quad {}_3\mathbf{u} = \left\{ \left(L + \frac{w}{2} \right), \left(\frac{L}{2} + w \right), 0 \right\} \cdot 10^{-3} \text{ mm}, \tag{87}$$

$${}_4\mathbf{u} = \left\{ \frac{w}{2}, w, 0 \right\} \cdot 10^{-3} \text{ mm}$$

The analytical solution for the strains [38]

$$\epsilon_{11} = \epsilon_{22} = \frac{1}{2} \epsilon_{12} = 10^{-3} \tag{88}$$

is matched exactly by DKQ-5 at the Gauss points. The same geometry can also be used in the bending patch test. Unfortunately, DKQ-5 does not pass the bending patch test.

6.3. Hemispherical shell: linear analysis

Convergence analysis for a double-curved hemispherical shell with a hole was performed. Due to the symmetry, see Fig. 10, only one quarter of the hemispherical shell was meshed and appropriate boundary conditions were taken into account. For the mesh edge “support I” in Fig. 10(a), the displacement in the y-direction and rotation around the edge are zero (displacement in the z-direction at the top node of that edge is also zero), and for the “support II” edge, the displacement in the x-direction and rotation around the edge are restrained. The following data were used:

$$R = 10 \text{ mm}, \quad \varphi = 72^\circ, \quad h = 0.04 \text{ mm}, \quad r = 16, \tag{89}$$

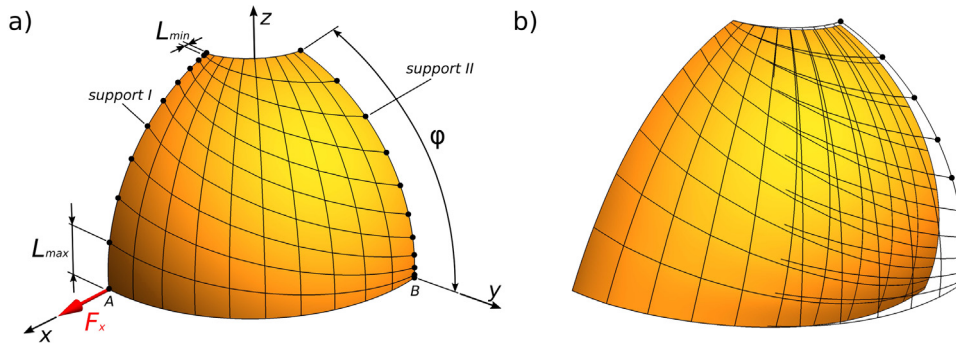


Fig. 10. Hemispherical shell: (a) undeformed and (b) deformed configuration meshed with 10×10 elements (scaling factor is 10).

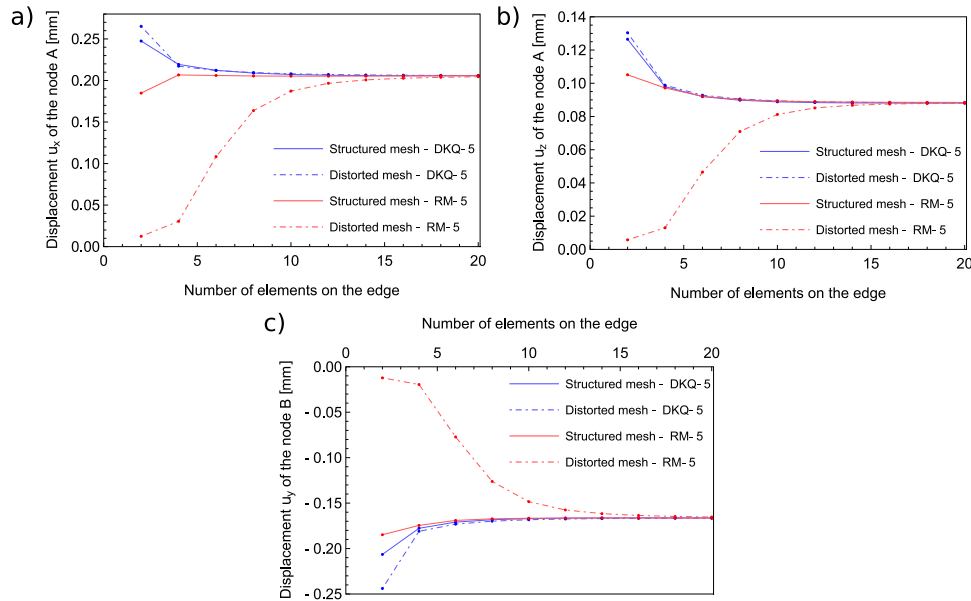


Fig. 11. Hemispherical shell: convergence plots for (a) displacement of node A in x direction, (b) displacement of node A in z direction, and (c) displacement of node B in y direction.

$$E = 6.825 \cdot 10^7 \text{ MPa}, \quad \nu = 0.3, \quad F_x = 4 \text{ N}.$$

Note that only one force is applied to one quarter of the shell, which is in contrast to the standard benchmark test, see e.g. [38] and [39], where one inward and one outward forces are applied.

The convergence of the displacements at nodes A and B (see Fig. 10) is shown in Fig. 11. In all cases the mesh consisted of $n \times n$ elements. We can see that RM-5 converges slightly better than DKQ-5 for the structured mesh, but it is much worse for the distorted mesh. In fact, the DKQ-5 convergence properties for the distorted mesh change only slightly in comparison with the structured mesh. The converged values for the displacements from Fig. 11 are 0.206, 0.088 and -0.166 mm, respectively.

6.4. Pinched cylinder: linear analysis

We consider a pinched cylinder, studied before in e.g. [1] and [40]. In Fig. 12, a mesh for one eighth of the cylinder is shown that can be applied (with appropriate boundary conditions) because of the symmetry. The following boundary displacements and rotations are set to zero: at the mesh edge “support I”, the displacement in the y-direction and rotation around the edge; at “support II”, the displacement in the x-direction and rotation around the edge; at “support III”, the displacements in the x and z-directions; and at “support IV”, the displacement in the z-direction and rotation around the edge. The geometric and

material properties are:

$$R = 300 \text{ mm}, \quad w = 300 \text{ mm}, \quad h = 3 \text{ mm}, \quad r = 16, \quad (90)$$

$$E = 3 \cdot 10^6 \text{ MPa}, \quad \nu = 0.3, \quad F_z = -2.5 \cdot 10^4 \text{ N}.$$

Convergence plots for the displacements at nodes A and B, see Fig. 12(a), are shown in Fig. 13. The mesh consisted of $n \times n$ elements in all cases. For a structured mesh, convergence with DKQ-5 and RM-5 is reached with 10×10 and 18×18 meshes, respectively. For distorted mesh, this happens for 18×18 and 26×26 meshes. The converged displacements for Fig. 13(a) and (b) are $-4.929 \cdot 10^{-3}$ and -1.825 mm.

6.5. Twisted beam: linear analysis

The twisted beam example has been studied in e.g. [41] and [40]. The beam in Fig. 14 is clamped at one end and subjected to a force at the other end. Its cross-section is horizontal at the clamped edge and twisted by $\frac{\pi}{2}$ around x where the force acts. The meshes consist of $n \times m$ elements, with $m = 6 \times n$. The rest of the geometric and material data are:

$$L = 12 \text{ mm}, \quad w = 1.1 \text{ mm}, \quad h = 0.0032 \text{ mm}, \quad r = 2, \quad (91)$$

$$E = 29 \cdot 10^6 \text{ MPa}, \quad \nu = 0.22, \quad F_y = 1 \cdot 10^{-6} \text{ N}.$$

Fig. 15 shows the convergence of displacements in the y and z-direction at node A. For displacements at Fig. 15(a) and (b), the

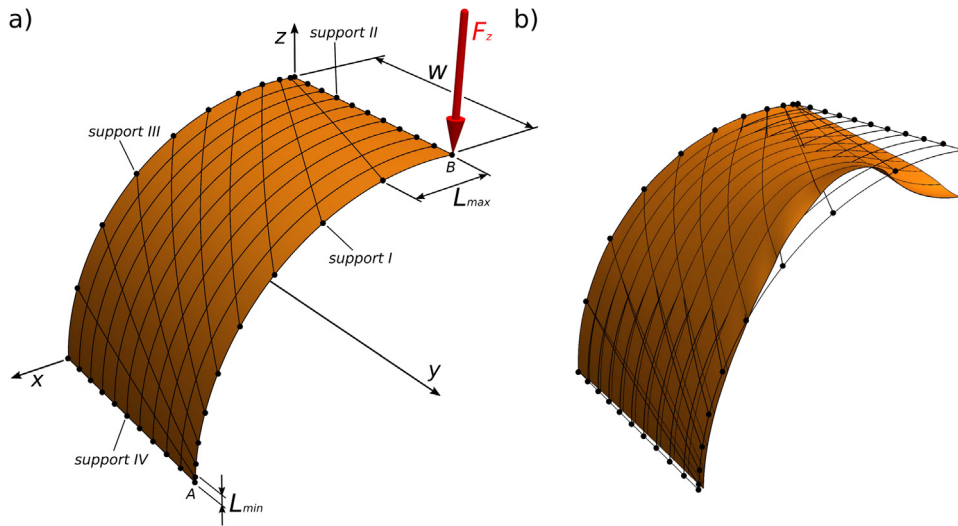


Fig. 12. Pinched cylinder: (a) undeformed and (b) deformed configurations meshed with 10×10 elements (scaling factors is 30).

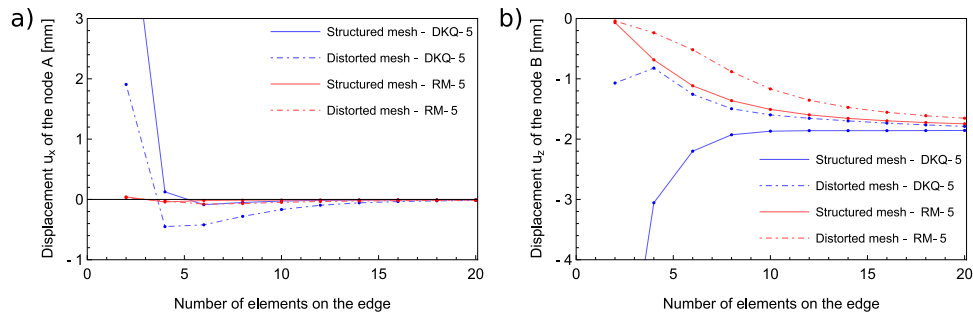


Fig. 13. Pinched cylinder: convergence plots for (a) displacement at node A in x direction, and (b) displacement at node B in z direction.

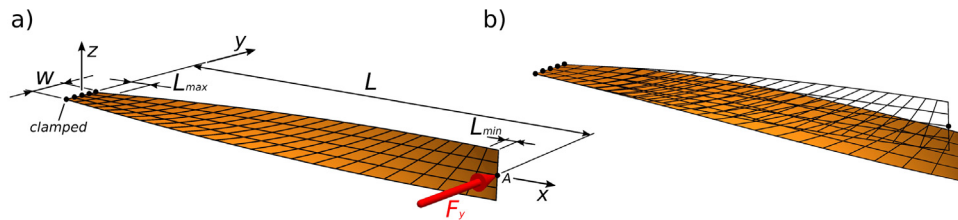


Fig. 14. Twisted beam: (a) undeformed and (b) deformed configuration meshed with 4×24 elements (scaling factor is 500).

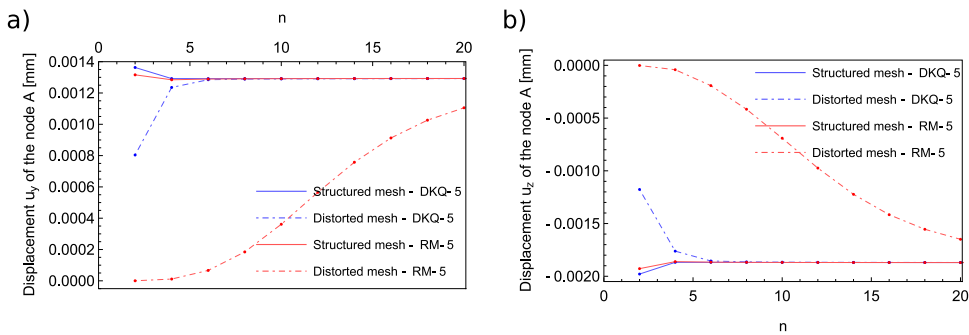


Fig. 15. Twisted beam convergence plot for: (a) displacement of node A in y, (b) displacement of node A in z.

converged values are $1.29 \cdot 10^{-3}$ and $-1.87 \cdot 10^{-3}$ mm. For structured mesh, both elements reach convergence with 4×24 elements. For distorted mesh, RM-5 performs very poorly, and it converges only for fine mesh of 40×240 elements. On the other hand, DKQ-5 reaches

convergence already with mesh 6×36 . Note that if the mesh distortion is increased to $r = 16$, DKQ-5 needs twice denser mesh of 12×72 elements to converge, while RM-5 needs extremely fine mesh of 120×720 elements.

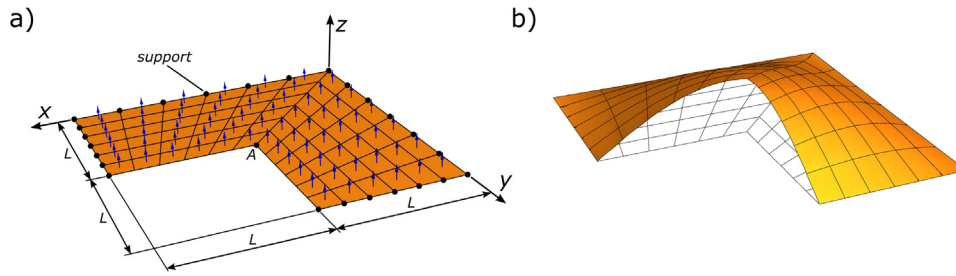


Fig. 16. L-shaped plate: (a) undeformed and (b) deformed configuration meshed with $6 \times 6 \times 2$ elements (scaling factor is 0.01).

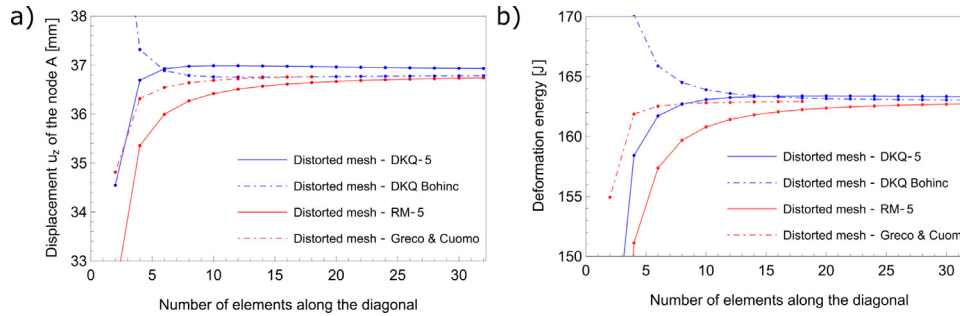


Fig. 17. L-shaped plate convergence plot for: (a) displacement of node A in z-direction, (b) deformation energy.

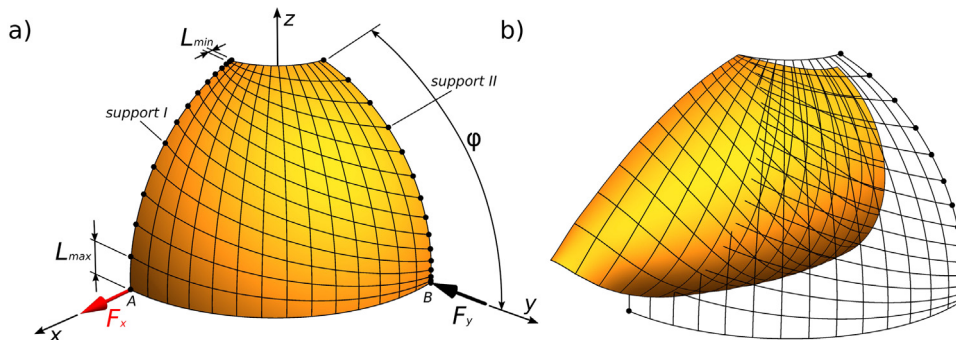


Fig. 18. Hemispherical shell, nonlinear analysis: (a) undeformed and (b) deformed configuration meshed with 14×14 elements.

6.6. L-shaped plate: linear analysis

The L-shaped plate has been studied in e.g. [7]. The plate in Fig. 16 is simply supported at all exterior edges and free at the two interior edges. It is subjected to the uniform pressure. The mesh consists of $n \times n \times 2$ distorted finite elements. The geometrical and material properties are:

$$L = 1 \text{ m}, \quad h = 1 \cdot 10^{-4} \text{ m}, \quad p = 7.848 \text{ Pa}, \quad (92)$$

$$E = 200 \cdot 10^9 \text{ Pa}, \quad \nu = 0.3.$$

Fig. 17(a) shows the convergence of displacement in the z-direction at node A and Fig. 17(b) convergence of the deformation energy of the system. The results of DKQ-5 are compared with discrete Kirchhoff plate element (DKQ) described in [42], RM-5, and shell finite element from [7]. All elements converge to displacement 36.817 mm and deformation energy 162.992 J, computed with a mesh of $500 \times 500 \times 2$ DKQ elements. The DKQ-5 convergence is the slowest. We may conclude that the reason for poor convergence of DKQ-5 in this example is the singularity in the re-entrant corner. The singularity point influences DKQ-5 more than other formulations.

6.7. Hemispherical shell

A nonlinear analysis of hemispherical shell, a popular benchmark test [43] and [39], was performed. In Fig. 18(a), the geometry of one quarter of the hemisphere is shown with the displacement/rotation boundary conditions, which are the same as in Example 6.3. We note, however, that two forces are acting on one quarter of the shell in the nonlinear example. Geometrical and material data are also the same, only force F_y is added:

$$R = 10 \text{ mm}, \quad \phi = 72^\circ, \quad h = 0.04 \text{ mm}, \quad r = 16, \quad (93)$$

$$E = 6.825 \cdot 10^7 \text{ MPa}, \quad \nu = 0.3, \quad F_x = -F_y.$$

In Fig. 18(b), the deformed configuration is shown. The DKQ-5 and RM-5 results are compared with reference results from [43] in Fig. 19: displacements at nodes A and B are shown for mesh 14×14 . Fig. 19(a) shows the results for the structured mesh, and Fig. 19(b) shows the results for the distorted mesh. We can see that DKQ-5 matches well the reference values, while RM-5 does not. For the distorted mesh, the difference between DKQ-5 (which is in good agreement with the reference values) and RM-5 is even more pronounced.

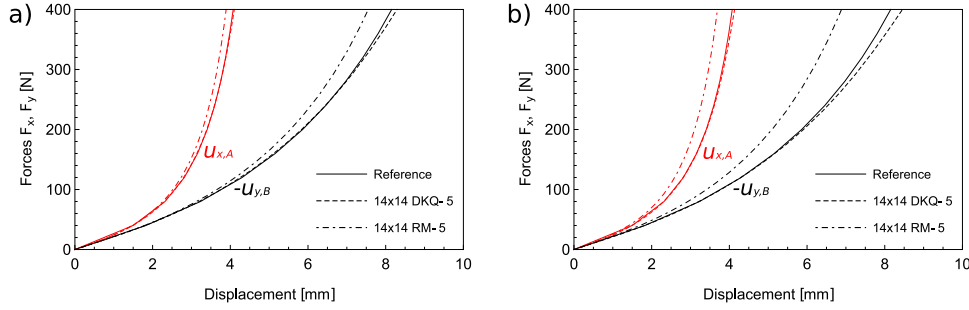


Fig. 19. Hemisphere shell, nonlinear analysis: displacement comparison for (a) structured mesh and (b) distorted mesh.

6.8. Cylindrical panel

One-edge-clamped cylindrical panel is loaded with line moment as shown in Fig. 20(a). The geometrical and material parameters are taken from [4]:

$$\begin{aligned} R = 20 \text{ mm}, \quad w = 10 \text{ mm}, \quad \varphi = 30^\circ, \quad h = 0.002 \text{ mm}, \\ r = 12, \quad E = 2.1 \cdot 10^6 \text{ MPa}, \quad \nu = 0.0. \end{aligned} \quad (94)$$

With Poisson's ratio set to zero, this is a pure one-dimensional bending test.

In Fig. 20(b), the deformed configuration of the pinched cylinder is shown for the 4×4 mesh. The displacements at node A are shown in Fig. 21 for both structured and distorted 4×4 mesh. For structured mesh, the DKQ-5 curves match the reference curves, while the RM-5 curves differ from the reference ones (although not shown, they get much closer for the 8×8 mesh). For the distorted mesh, DKQ-5 still behaves excellently, while RM-5 totally fails. Note that very fine 80×80 distorted mesh is needed for RM-5 to match the reference curves, while DKQ-5 matches them quite well already for the 8×8 mesh.

6.9. Twisted beam

The twisted beam example from Section 6.5 is also used for the nonlinear analysis, and the results are compared with those from [43]. We use structured and distorted 4×24 mesh. Two load cases are considered, shown in Figs. 22 and 24. The geometrical and material parameters are:

$$\begin{aligned} L = 12 \text{ mm}, \quad w = 1.1 \text{ mm}, \quad h = 0.0032 \text{ mm}, \\ r = 2, \quad E = 29 \cdot 10^7 \text{ MPa}, \quad \nu = 0.22. \end{aligned} \quad (95)$$

Fig. 23 shows displacement curves for node A for the first loading case. For the structured mesh, the DKQ-5 curves align very well with the reference curves from [43]. A similarly good match is obtained also for the RM-5 curves for displacement u_z , but not for displacement u_y (we note that the latter RM-5 curve almost perfectly aligns with the reference one for denser 12×72 mesh). For the distorted mesh, the DKQ-5 curves still match very well with the reference curves. On the other end, the RM-5 curves differ significantly (and come close to the reference ones only for very fine 32×192 mesh). Fig. 25 presents displacements at node A for the second load case. For the structured mesh, DKQ-5 shows very good alignment with the reference curves (practically perfect alignment is reached for the 8×48 mesh). On the other hand, the RM-5 results differ from the reference curves considerably (although not shown, they come very close only for fine 16×96 mesh). For the distorted mesh, the RM-5 results are extremely poor and the convergence is lost, while mesh distortion does not affect the DKQ-5 results at all (note that for mesh refinement to 8×48 elements, we reach a practically perfect alignment between DKQ-5 and reference curves).

6.10. Helical beam

Following [4], we analyse clamped beam with cross section rotating by 360° along the beam axis, see Fig. 26(a), where the loading is also shown. The following geometrical and material data apply:

$$\begin{aligned} L = 10 \text{ mm}, \quad w = 4 \text{ mm}, \quad h = 0.0032 \text{ mm}, \\ r = 2, \quad E = 29 \cdot 10^6 \text{ MPa}, \quad \nu = 0.22. \end{aligned} \quad (96)$$

We used structured and distorted meshes with 6×20 finite elements. The DKQ-5 curves in Fig. 27 match very well the reference curves for both, structured and unstructured mesh. On the other hand, the RM-5 results for the distorted mesh are very poor: zero displacement in the y -direction and linearly varying displacement in the z -direction are computed for the increasing load and unstructured mesh, while for the structured mesh they show a rather good match. Note that DKQ-5 yields a practically perfect alignment with the reference curves for both structured and distorted meshes when 12×40 elements are used, and RM-5 yields a good match with the reference curves for 12×40 structured mesh and 30×100 distorted mesh.

6.11. Raasch's hook

Raasch's hook is a difficult test for shell finite elements, see e.g. [4] and [43]. The hook is clamped at one edge and subjected to point force at the opposite edge, see Fig. 28. The hook was meshed with $(2N+3N) \times N$ finite elements, where N is a number of elements across the width of the hook, $2N$ is a number of elements across radius r , and $3N$ is a number of elements across radius R . Used material and geometrical data were the same as in [4]:

$$\begin{aligned} R = 46 \text{ mm}, \quad r = 14 \text{ mm}, \quad w = 20 \text{ mm}, \quad \varphi = 150^\circ, \\ \beta = 60^\circ, \quad h = 0.02 \text{ mm}, \quad r_R = 2, \quad r_r = 1.5, \\ E = 3.3 \cdot 10^3 \text{ MPa}, \quad \nu = 0.3, \end{aligned} \quad (97)$$

The results are presented in Fig. 29, where displacements at node A in the x and z directions are shown. For Fig. 29(a), a structured mesh with $(8+12) \times 4$ elements was used, and for Fig. 29(b), the same number of elements were used for distorted mesh with distortion factors r_R and r_r . From Fig. 29(a) we can see a noticeable difference from the reference curves for the DKQ-5 element. The RM-5 curves differ even more from the reference curves. From Fig. 29(b) we can observe that mesh distortion does not influence much the DKQ-5 results. On the contrary, RM-5 results suffer a lot from the mesh distortion. For a denser mesh with $N = 16$, we get an excellent match with the reference results from [4] for DKQ-5.

6.12. Hemisphere on elastic substrate

In the final example, we test our finite element formulation on a hemisphere, attached to an elastic foundation. We want to check if the DKQ-5 results are comparable with those presented in the [25],

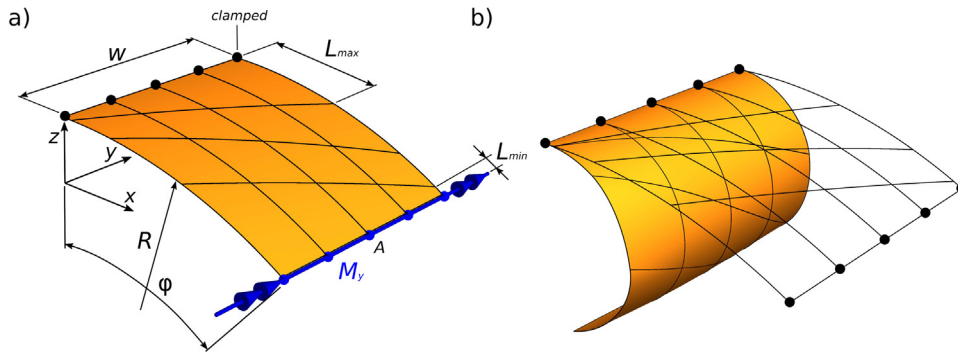


Fig. 20. Cylindrical panel, nonlinear analysis: (a) undeformed and (b) deformed configuration meshed with 4×4 elements.

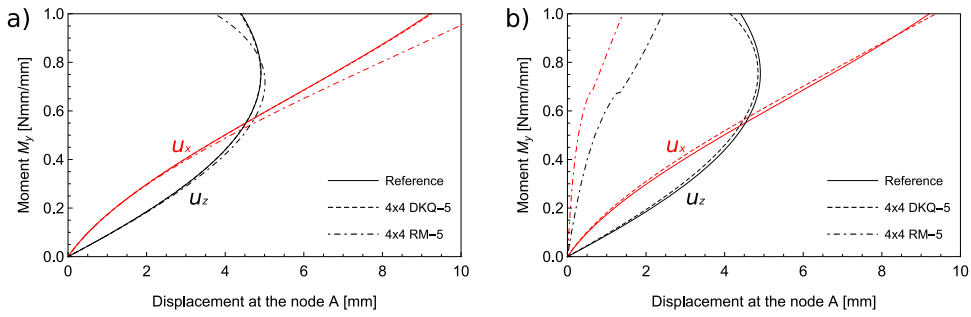


Fig. 21. Cylindrical panel, nonlinear analysis: displacement comparison for (a) structured mesh and (b) distorted mesh.

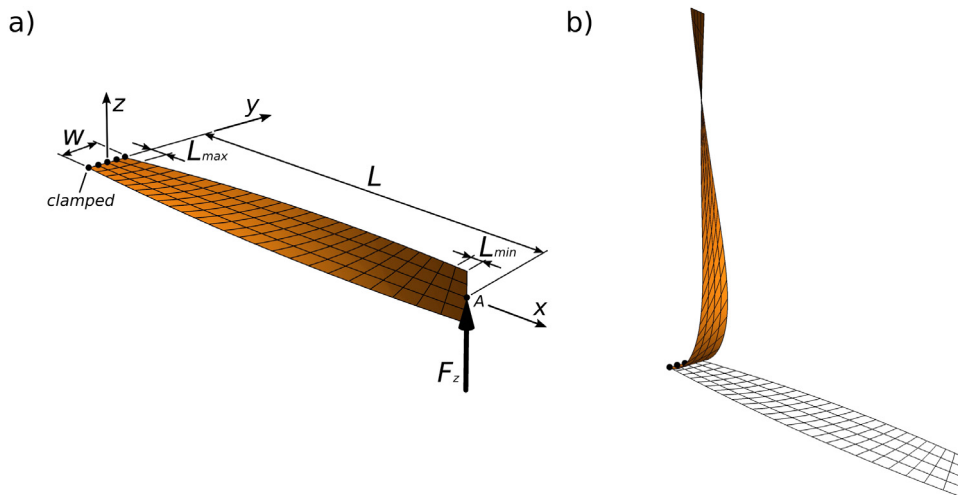


Fig. 22. Twisted beam, nonlinear analysis for vertical load: (a) undeformed and (b) deformed configurations meshed with 4×24 elements.

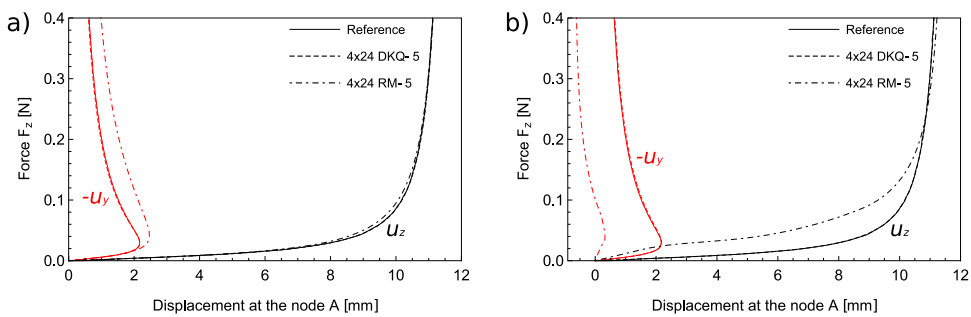


Fig. 23. Twisted beam, nonlinear analysis for vertical load: displacement comparison for (a) structured mesh and (b) distorted mesh.

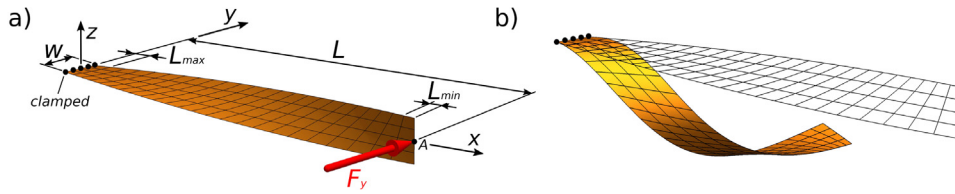


Fig. 24. Twisted beam, nonlinear analysis for horizontal load: (a) undeformed and (b) deformed configuration meshed with 4×24 elements.

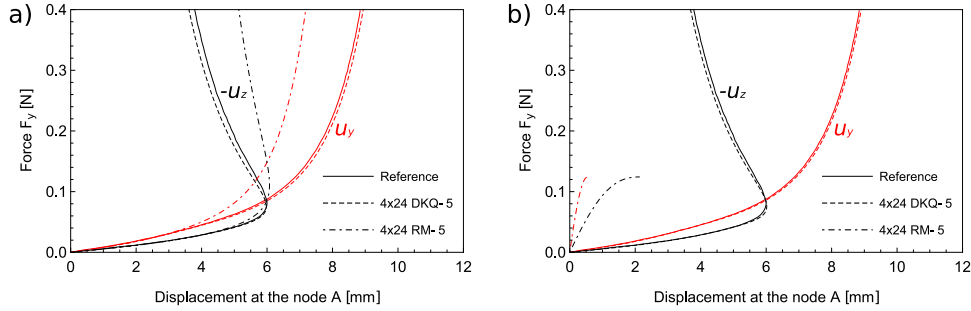


Fig. 25. Twisted beam, nonlinear analysis for horizontal load: displacement comparison for (a) structured mesh and (b) distorted mesh.

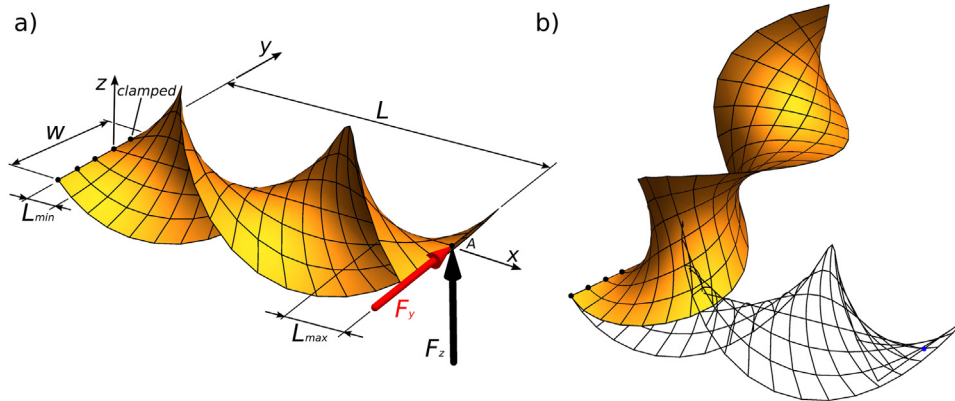


Fig. 26. Helical beam: (a) undeformed and (b) deformed configurations meshed with 6×20 elements.

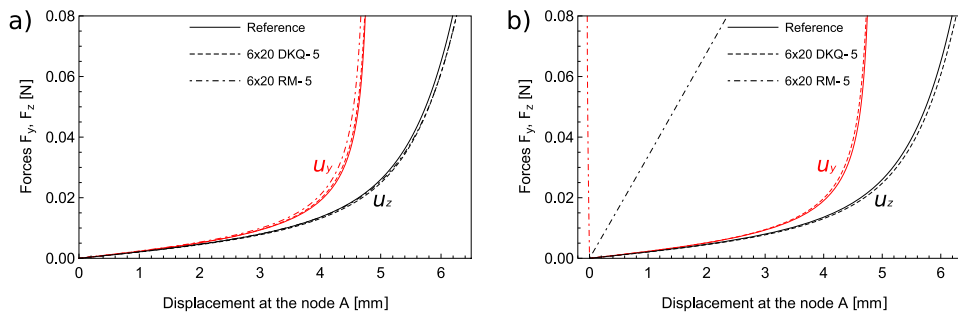


Fig. 27. Helical beam: displacement comparison for (a) structured mesh and (b) distorted mesh.

where a special-purpose element was used. The material and geometric parameters are:

$$R = 20 \text{ mm}, \quad h = \{0.4, 0.6, 0.8, 1.0\} \text{ mm}, \quad E = 2.1 \text{ MPa}, \quad (98)$$

$$\nu = 0.49, \quad K_s = \{0.2610, 0.1738, 0.1302, 0.1039\} \text{ N/mm}^3.$$

where K_s is the stiffness of elastic foundation (that has direction towards the centre of the radius of the hemisphere) representing the substrate. As the parameter set (98) suggests, four different cases are solved. Only for the purpose of this example, the element formulation

was redesigned in order to have displacements in the nodes of DKQ-5 finite element in the local orthonormal coordinate systems ${}_1E_1, {}_1E_2, {}_1A_3$. This enabled restraining the displacements in the tangential direction on the bottom edge of the shell (both rotations were restrained too). The path-following method [44] was used to compute the solution. There are multiple buckling modes close to one another, but we managed to get the one with the minimal energy by using the fact that the meshing can be never symmetric for the half-sphere (due to Euler's

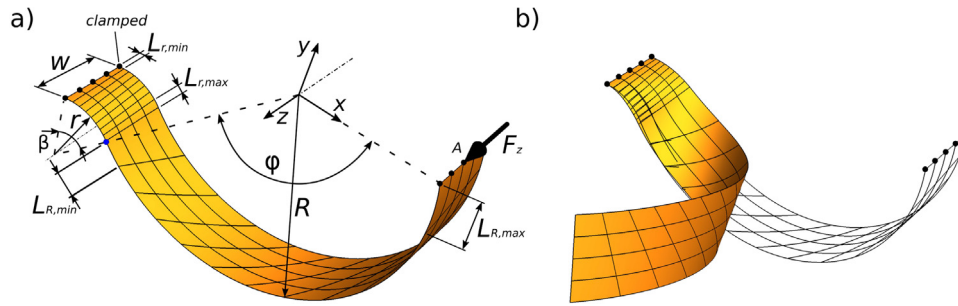


Fig. 28. Raasch's hook: (a) undeformed and (b) deformed configurations of the mesh with $(8 + 12) \times 4$ finite elements.

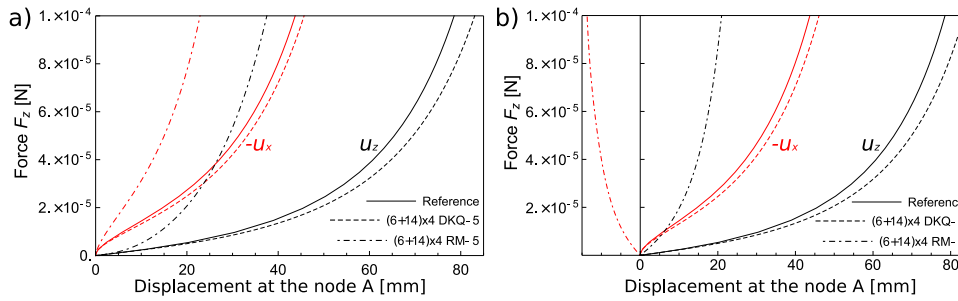


Fig. 29. Raasch's hook: displacement comparison for (a) structured mesh and (b) distorted mesh.

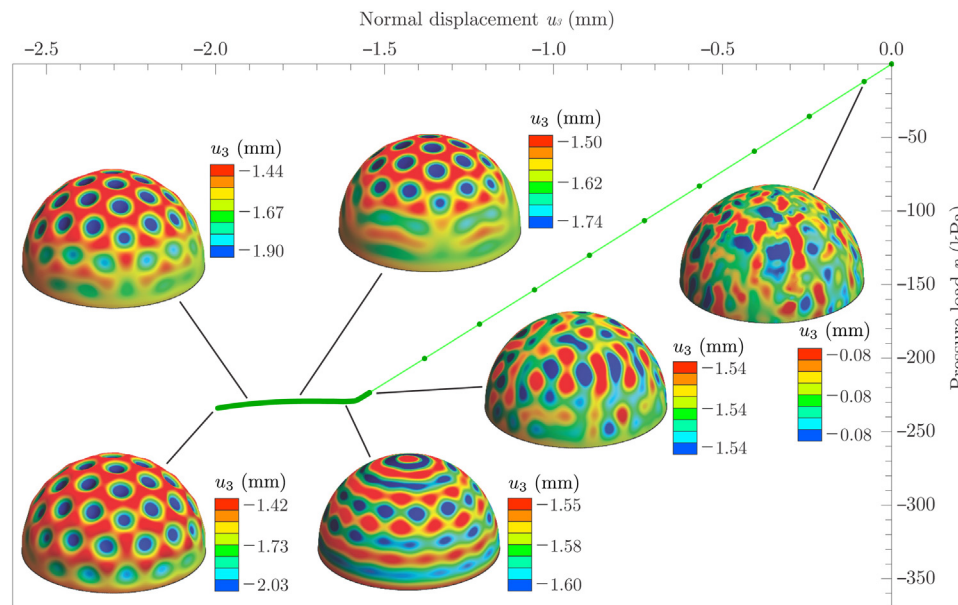


Fig. 30. Development of the normal displacement field u_3 on the hemisphere under pressure p . The data are: $R = 20.0$ mm, $h = 0.8$ mm, $E = 2.1$ MPa, $\nu = 0.49$ mm, $K_s = 0.1302$ N/mm³, and the number of elements is 148512.

theorem on tessellations by polygons), which imposes an initial mesh-imperfections that change the first bifurcation point into the limit point.

In Fig. 30, the evolution of the wrinkling pattern of the hemisphere is shown for the thickness of the shell $h = 0.8$ mm. By comparing Fig. 30 with the results from [25], we found that dimpled pattern starts to form at approximately the same pressure (i.e. $p \approx -238$ kPa). We also found that the distances between the dimples are similar. In addition to the results shown in Fig. 30, we also performed analysis for three other cases. In Fig. 31, the final deformation configurations are shown for all four analysis. For each case, we counted the number of dimples, calculated the average characteristic wavelength and its standard deviation. The number of dimples

(left to right with respect to Fig. 31) was (227, 97, 56, 33), the average characteristic wavelength was $\lambda = (3.522, 5.250, 6.959, 8.675)$ mm and the standard deviation was (0.374, 0.245, 0.338, 0.411) mm for each element of the parameter set. Theoretically calculated wavelengths (see [45]) are $\lambda = (3.642, 5.463, 7.283, 9.104)$ mm, which means that only (3.3, 3.9, 4.4, 4.7) % relative difference is obtained via our numerical procedure. For example in [25], the average characteristic wavelengths for the same cases, as shown in the Fig. 31, are $\lambda = (3.488, 5.149, 6.988, 8.552)$ mm with standard deviation (0.317, 0.425, 0.528, 0.817) mm. The relative difference compared to the theoretically calculated values are (4.2, 5.7, 4.1, 6.1) %. From the relative difference, we can see that for almost all cases the DKQ-5 finite element model

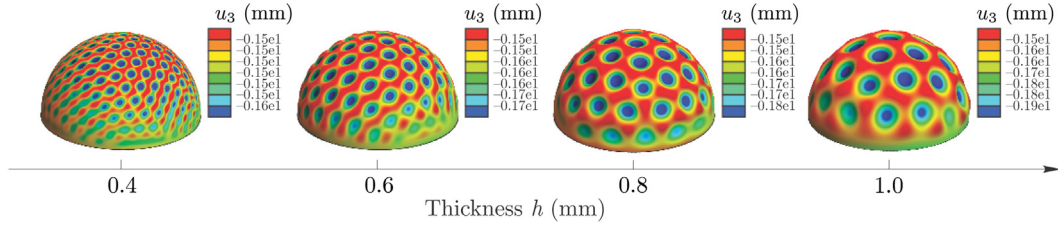


Fig. 31. Fully developed wrinkling patterns on the hemispheres for different K_s and h .

gives slightly better results than the model presented in [25]. The exception is only the 3rd case with thickness $h = 0.8$ mm.

7. Conclusion

We have applied the concepts of the discrete Kirchhoff formulations (classically used for derivation of near optimal plate elements) to derive a non-linear discrete Kirchhoff–Love four-node quadrilateral shell finite element. The element uses interpolations that yield from the cubic Hermite curves and bilinear Coons surface patch and impose the G^1 -continuity at the nodes. The major advantage of the presented formulation, with respect to the full Kirchhoff–Love shell formulations, is that it has less dofs/nodes. In fact, the element has 5 degrees of freedom per node, three displacements and two rotations, i.e. the same number as the standard Reissner–Mindlin shell quadrilaterals (cf. e.g. MITC4 evaluated in e.g. [4]), but satisfies more stringent demands on the geometric continuity of the approximated shell mid-surface. The rotational degrees of freedom rotate the nodal tangent plane to the mid-surface as well as the nodal normal-to-the-mid-surface unit vector. The presented element uses the same data as the Reissner–Mindlin quadrilaterals to construct the mesh: nodal coordinates and mid-surface normal vector. The advantages of the present element over the Reissner–Mindlin formulations are the complete elimination of the transverse shear deformations and thus the elimination of the shear locking. Also the implementation of the hyperelastic and (elastoplastic) material models (given in terms of principal stretches) can be simpler.

There have been a very few attempts to construct nonlinear discrete Kirchhoff–Love shell quadrilaterals. As shown in this work, this is not quite straightforward, an important issue being membrane locking. In order to eliminate the membrane locking, we used assumed natural strain method proposed in [3], which also makes quadrilateral shell formulations less sensitive to mesh distortion (as shown, e.g., in [4]). Our numerical experiments indicate that the derived element is almost insensitive to mesh distortion as long as the distortion is not too extreme. The element has six zero eigenvalues and passes the membrane patch test. As for the bending patch test, it passes it for the structured meshes but fails it for the distorted meshes, which is a common problem of shell elements with higher-order interpolation. Nevertheless, the performance of the derived element in linear and non-linear settings is very good. The results of simulations on the shell–substrate systems shown that the derived element can also be successfully used to solve wrinkling problems. The presented discrete Kirchhoff–Love shell formulation can be seen as a step towards a G^1 -conforming Kirchhoff–Love shell element that exploits surface patches and possesses G^1 -continuity along the complete boundary of the element.

CRedit authorship contribution statement

Tomó Veldin: Conceptualization, Methodology, Software, Investigation, Writing – original draft. **Boštjan Brank:** Conceptualization, Supervision, Writing – review & editing. **Miha Brojan:** Supervision, Writing – review & editing.

Declaration of competing interest

The authors declare that they have no known competing financial interests or personal relationships that could have appeared to influence the work reported in this paper.

Acknowledgments

We thank Dr. M. Lavrenčič for helpful discussions regarding numerical examples, and Profs. A. Peperko and G. Jaklič for helping us with calculus of variations and geometric modelling. B.B. and M.B. gratefully acknowledge the financial support of the Slovenian Research Agency (project grant numbers J2-1722, J2-2490 and J2-9223).

Appendix

A.1. Solution of the curve functional

The functional is defined in (25) and the accompanying boundary conditions are given in (27). By writing the Lagrange function

$$L = L(t, \mathbf{R}(t), \mathbf{R}(t)', \mathbf{R}(t)'') = \mathbf{R}(t)' \cdot \mathbf{R}(t)'', \quad (99)$$

$\mathbf{R}(t)$ can be found from the condition:

$$\delta I(\mathbf{R}) = \int_{t_0}^{t_1} \delta L(t, \mathbf{R}(t), \mathbf{R}(t)', \mathbf{R}(t)'') dt = 0. \quad (100)$$

Variation of the Lagrange function is

$$\delta L = \frac{\partial L}{\partial \mathbf{R}} \cdot \delta \mathbf{R} + \frac{\partial L}{\partial \mathbf{R}'} \cdot \delta \mathbf{R}' + \frac{\partial L}{\partial \mathbf{R}''} \cdot \delta \mathbf{R}'' . \quad (101)$$

If (101) is inserted into (100), we get

$$\delta I(\mathbf{R}) = \int_{t_0}^{t_1} \left(\frac{\partial L}{\partial \mathbf{R}} \cdot \delta \mathbf{R} + \frac{\partial L}{\partial \mathbf{R}'} \cdot \delta \mathbf{R}' + \frac{\partial L}{\partial \mathbf{R}''} \cdot \delta \mathbf{R}'' \right) dt = 0, \quad (102)$$

where $\delta \mathbf{R}' = d\delta \mathbf{R}/dt$, and $\delta \mathbf{R}'' = d^2\delta \mathbf{R}/dt^2$. We integrate the second and the third expression inside the brackets in (102) by parts. First we integrate by parts the second expression

$$\begin{aligned} \int_{t_0}^{t_1} \frac{\partial L}{\partial \mathbf{R}'} \cdot \delta \mathbf{R}' dt &= \\ \int_{t_0}^{t_1} \frac{\partial L}{\partial \mathbf{R}'} \cdot \frac{d\delta \mathbf{R}}{dt} dt &= \left[\frac{\partial L}{\partial \mathbf{R}'} \cdot \delta \mathbf{R} \right]_{t_0}^{t_1} - \int_{t_0}^{t_1} \delta \mathbf{R} \cdot \frac{d}{dt} \left(\frac{\partial L}{\partial \mathbf{R}'} \right) dt. \end{aligned} \quad (103)$$

We proceed by integrating by parts the third expression

$$\begin{aligned} \int_{t_0}^{t_1} \frac{\partial L}{\partial \mathbf{R}''} \cdot \delta \mathbf{R}'' dt &= \\ \int_{t_0}^{t_1} \frac{\partial L}{\partial \mathbf{R}''} \cdot \frac{d^2\delta \mathbf{R}}{dt^2} dt &= \left[\frac{\partial L}{\partial \mathbf{R}''} \cdot \frac{d\delta \mathbf{R}}{dt} \right]_{t_0}^{t_1} \\ &\quad - \int_{t_0}^{t_1} \frac{d\delta \mathbf{R}}{dt} \cdot \frac{d}{dt} \left(\frac{\partial L}{\partial \mathbf{R}''} \right) dt. \end{aligned} \quad (104)$$

We further integrate by parts the second expression in (104)

$$\int_{t_0}^{t_1} \frac{\partial L}{\partial \mathbf{R}''} \cdot \frac{d^2\delta \mathbf{R}}{dt^2} dt =$$

$$\left[\frac{\partial L}{\partial \mathbf{R}''} \cdot \frac{d\delta \mathbf{R}}{dt} \right]_{t_0}^{t_1} - \left[\frac{d}{dt} \left(\frac{\partial L}{\partial \mathbf{R}''} \right) \cdot \delta \mathbf{R} \right]_{t_0}^{t_1} + \int_{t_0}^{t_1} \frac{d^2}{dt^2} \left(\frac{\partial L}{\partial \mathbf{R}''} \right) \cdot \delta \mathbf{R} dt. \tag{105}$$

Now we can reorganize (102) as

$$\delta I(\mathbf{R}) = \int_{t_0}^{t_1} \frac{\partial L}{\partial \mathbf{R}} \cdot \delta \mathbf{R} dt + \left[\frac{\partial L}{\partial \mathbf{R}'} \cdot \delta \mathbf{R} \right]_{t_0}^{t_1} - \int_{t_0}^{t_1} \delta \mathbf{R} \cdot \frac{d}{dt} \left(\frac{\partial L}{\partial \mathbf{R}'} \right) dt + \left[\frac{\partial L}{\partial \mathbf{R}''} \cdot \frac{d\delta \mathbf{R}}{dt} \right]_{t_0}^{t_1} - \left[\frac{d}{dt} \left(\frac{\partial L}{\partial \mathbf{R}''} \right) \cdot \delta \mathbf{R} \right]_{t_0}^{t_1} + \int_{t_0}^{t_1} \frac{d^2}{dt^2} \left(\frac{\partial L}{\partial \mathbf{R}''} \right) \cdot \delta \mathbf{R} dt = 0, \tag{106}$$

and rewrite the above to get

$$\delta I(\mathbf{R}) = \left[\frac{\partial L}{\partial \mathbf{R}'} \cdot \delta \mathbf{R} \right]_{t_0}^{t_1} + \left[\frac{\partial L}{\partial \mathbf{R}''} \cdot \frac{d\delta \mathbf{R}}{dt} \right]_{t_0}^{t_1} - \left[\frac{d}{dt} \left(\frac{\partial L}{\partial \mathbf{R}''} \right) \cdot \delta \mathbf{R} \right]_{t_0}^{t_1} + \int_{t_0}^{t_1} \left(\frac{\partial L}{\partial \mathbf{R}} - \frac{d}{dt} \left(\frac{\partial L}{\partial \mathbf{R}'} \right) + \frac{d^2}{dt^2} \left(\frac{\partial L}{\partial \mathbf{R}''} \right) \right) \cdot \delta \mathbf{R} dt = 0. \tag{107}$$

Based on (107), we can write the necessary conditions in the form of Euler–Lagrange equation as:

$$\frac{\partial L}{\partial \mathbf{R}} - \frac{d}{dt} \left(\frac{\partial L}{\partial \mathbf{R}'} \right) + \frac{d^2}{dt^2} \left(\frac{\partial L}{\partial \mathbf{R}''} \right) = \mathbf{0}. \tag{108}$$

In (108) we need the following derivatives

$$\frac{\partial L}{\partial \mathbf{R}} = 2 \frac{\partial \mathbf{R}''}{\partial \mathbf{R}} \cdot \mathbf{R}'' = \mathbf{0}, \tag{109}$$

$$\frac{\partial L}{\partial \mathbf{R}'} = 2 \frac{\partial \mathbf{R}''}{\partial \mathbf{R}'} \cdot \mathbf{R}'' = \mathbf{0} \tag{110}$$

and

$$\frac{\partial L}{\partial \mathbf{R}''} = 2 \mathbf{R}'' \tag{111}$$

Eqs. (109)–(111) are inserted into Euler–Lagrange equation (108) to get

$$\frac{d^2}{dt^2} (2\mathbf{R}'') = 2\mathbf{R}'''' = \mathbf{0}, \tag{112}$$

The solution of the differential equation of the 4th order $\mathbf{R}(t)'''' = \mathbf{0}$ is

$$\mathbf{R}(t) = t^3 \mathbf{C}_4 + t^2 \mathbf{C}_3 + t \mathbf{C}_2 + \mathbf{C}_1. \tag{113}$$

We write also natural boundary conditions based on Eq. (107)

$$\left[\frac{\partial L}{\partial \mathbf{R}'} \cdot \delta \mathbf{R} \right]_{t_0}^{t_1} + \left[\frac{\partial L}{\partial \mathbf{R}''} \cdot \frac{d\delta \mathbf{R}}{dt} \right]_{t_0}^{t_1} - \left[\frac{d}{dt} \left(\frac{\partial L}{\partial \mathbf{R}''} \right) \cdot \delta \mathbf{R} \right]_{t_0}^{t_1} = 0. \tag{114}$$

Variations of geometrical boundary conditions written in Eq. (27) are

$$\delta \mathbf{R}(t_0) = \delta \mathbf{R}(t_1) = \delta \mathbf{R}'(t_0) = \delta \mathbf{R}'(t_1) = \mathbf{0}, \tag{115}$$

and Eq. (114) is trivially fulfilled.

A.2. Components of the covariant tangent basis vectors

The components of the covariant tangent basis vectors which we get by solving the system of Eqs. (38) are

$$\begin{aligned} \alpha_1^k = & \left(3 \left(4 \mathbf{I} \mathbf{E}_1 \cdot \mathbf{J} \mathbf{E}_1 (-\mathbf{J} \mathbf{E}_1 \cdot \mathbf{X}_I + \mathbf{J} \mathbf{E}_1 \cdot \mathbf{X}_J) - \right. \right. \\ & \mathbf{I} \mathbf{E}_1 \cdot \mathbf{J} \mathbf{E}_2 \mathbf{J} \mathbf{E}_1 \cdot \mathbf{I} \mathbf{E}_2 \mathbf{J} \mathbf{E}_1 \cdot \mathbf{X}_I \mathbf{I} \mathbf{E}_2 \cdot \mathbf{J} \mathbf{E}_2 + \mathbf{I} \mathbf{E}_1 \\ & \cdot \mathbf{J} \mathbf{E}_2 \mathbf{J} \mathbf{E}_1 \cdot \mathbf{I} \mathbf{E}_2 \mathbf{J} \mathbf{E}_1 \cdot \mathbf{X}_J \mathbf{I} \mathbf{E}_2 \cdot \mathbf{J} \mathbf{E}_2 + \\ & \mathbf{I} \mathbf{E}_1 \cdot \mathbf{J} \mathbf{E}_1 \mathbf{J} \mathbf{E}_1 \cdot \mathbf{X}_I (\mathbf{J} \mathbf{E}_2 \cdot \mathbf{J} \mathbf{E}_2)^2 - \mathbf{I} \mathbf{E}_1 \cdot \mathbf{J} \mathbf{E}_1 \mathbf{J} \mathbf{E}_1 \cdot \mathbf{X}_J (\mathbf{J} \mathbf{E}_2 \cdot \mathbf{J} \mathbf{E}_2)^2 - \\ & 2 \mathbf{I} \mathbf{E}_1 \cdot \mathbf{X}_I (-4 + (\mathbf{J} \mathbf{E}_1 \cdot \mathbf{I} \mathbf{E}_2)^2 + (\mathbf{I} \mathbf{E}_2 \cdot \mathbf{J} \mathbf{E}_2)^2) \\ & + 2 \mathbf{I} \mathbf{E}_1 \cdot \mathbf{X}_J (-4 + (\mathbf{J} \mathbf{E}_1 \cdot \mathbf{I} \mathbf{E}_2)^2 + (\mathbf{I} \mathbf{E}_2 \cdot \mathbf{J} \mathbf{E}_2)^2) + \\ & \left. \left. 2 \mathbf{I} \mathbf{E}_1 \cdot \mathbf{J} \mathbf{E}_1 \mathbf{J} \mathbf{E}_1 \cdot \mathbf{I} \mathbf{E}_2 \mathbf{I} \mathbf{E}_2 \cdot \mathbf{X}_I + 2 \mathbf{I} \mathbf{E}_1 \cdot \mathbf{J} \mathbf{E}_2 \mathbf{I} \mathbf{E}_2 \cdot \mathbf{J} \mathbf{E}_2 \mathbf{I} \mathbf{E}_2 \cdot \mathbf{X}_I - \right. \right. \end{aligned}$$

$$\begin{aligned} & 2 \mathbf{I} \mathbf{E}_1 \cdot \mathbf{J} \mathbf{E}_1 \mathbf{J} \mathbf{E}_1 \cdot \mathbf{I} \mathbf{E}_2 \mathbf{I} \mathbf{E}_2 \cdot \mathbf{X}_J - 2 \mathbf{I} \mathbf{E}_1 \cdot \mathbf{J} \mathbf{E}_2 \mathbf{I} \mathbf{E}_2 \cdot \mathbf{J} \mathbf{E}_2 \mathbf{I} \mathbf{E}_2 \cdot \mathbf{X}_J - \\ & 4 \mathbf{I} \mathbf{E}_1 \cdot \mathbf{J} \mathbf{E}_2 \mathbf{J} \mathbf{E}_2 \cdot \mathbf{X}_I + \mathbf{I} \mathbf{E}_1 \cdot \mathbf{J} \mathbf{E}_2 (\mathbf{J} \mathbf{E}_1 \cdot \mathbf{I} \mathbf{E}_2)^2 \mathbf{J} \mathbf{E}_2 \cdot \mathbf{X}_I - \\ & \mathbf{I} \mathbf{E}_1 \cdot \mathbf{J} \mathbf{E}_1 \mathbf{J} \mathbf{E}_1 \cdot \mathbf{I} \mathbf{E}_2 \mathbf{I} \mathbf{E}_2 \cdot \mathbf{J} \mathbf{E}_2 \mathbf{J} \mathbf{E}_2 \cdot \mathbf{X}_I \\ & + \left(-\mathbf{I} \mathbf{E}_1 \cdot \mathbf{J} \mathbf{E}_2 (-4 + (\mathbf{J} \mathbf{E}_1 \cdot \mathbf{I} \mathbf{E}_2)^2) + \right. \\ & \left. \mathbf{I} \mathbf{E}_1 \cdot \mathbf{J} \mathbf{E}_1 \mathbf{J} \mathbf{E}_1 \cdot \mathbf{I} \mathbf{E}_2 \mathbf{I} \mathbf{E}_2 \cdot \mathbf{J} \mathbf{E}_2 \right) \mathbf{J} \mathbf{E}_2 \cdot \mathbf{X}_J \Big) / \Omega, \tag{116} \end{aligned}$$

$$\begin{aligned} \alpha_2^k = & \left(3 \left((-4 + (\mathbf{J} \mathbf{E}_1 \cdot \mathbf{J} \mathbf{E}_2)^2) \mathbf{J} \mathbf{E}_1 \cdot \mathbf{I} \mathbf{E}_2 (\mathbf{J} \mathbf{E}_1 \cdot \mathbf{X}_I - \mathbf{J} \mathbf{E}_1 \cdot \mathbf{X}_J) \right. \right. \\ & + 2 \mathbf{I} \mathbf{E}_1 \cdot \mathbf{J} \mathbf{E}_2 \mathbf{I} \mathbf{E}_1 \cdot \mathbf{X}_I \mathbf{I} \mathbf{E}_2 \cdot \mathbf{J} \mathbf{E}_2 - 2 \mathbf{I} \mathbf{E}_1 \cdot \mathbf{J} \mathbf{E}_2 \mathbf{I} \mathbf{E}_1 \cdot \mathbf{X}_J \mathbf{I} \mathbf{E}_2 \cdot \mathbf{J} \mathbf{E}_2 \\ & + 8 \mathbf{I} \mathbf{E}_2 \cdot \mathbf{X}_I - \\ & 2 (\mathbf{J} \mathbf{E}_1 \cdot \mathbf{J} \mathbf{E}_2)^2 \mathbf{I} \mathbf{E}_2 \cdot \mathbf{X}_I - 8 \mathbf{I} \mathbf{E}_2 \cdot \mathbf{X}_J + 2 (\mathbf{J} \mathbf{E}_1 \cdot \mathbf{J} \mathbf{E}_2)^2 \mathbf{I} \mathbf{E}_2 \cdot \mathbf{X}_J - \\ & 4 \mathbf{I} \mathbf{E}_2 \cdot \mathbf{J} \mathbf{E}_2 \mathbf{J} \mathbf{E}_2 \cdot \mathbf{X}_I + (\mathbf{J} \mathbf{E}_1 \cdot \mathbf{J} \mathbf{E}_1)^2 (-2 \mathbf{I} \mathbf{E}_2 \cdot \mathbf{X}_I + 2 \mathbf{I} \mathbf{E}_2 \cdot \mathbf{X}_J + \\ & \mathbf{I} \mathbf{E}_2 \cdot \mathbf{J} \mathbf{E}_2 (\mathbf{J} \mathbf{E}_2 \cdot \mathbf{X}_I - \mathbf{J} \mathbf{E}_2 \cdot \mathbf{X}_J) \Big) + 4 \mathbf{I} \mathbf{E}_2 \cdot \mathbf{J} \mathbf{E}_2 \mathbf{J} \mathbf{E}_2 \cdot \mathbf{X}_J + \\ & \mathbf{I} \mathbf{E}_1 \cdot \mathbf{J} \mathbf{E}_1 \left(\mathbf{I} \mathbf{E}_1 \cdot \mathbf{J} \mathbf{E}_2 (-\mathbf{J} \mathbf{E}_1 \cdot \mathbf{X}_I + \mathbf{J} \mathbf{E}_1 \cdot \mathbf{X}_J) \mathbf{I} \mathbf{E}_2 \cdot \mathbf{J} \mathbf{E}_2 + \right. \\ & \left. \mathbf{J} \mathbf{E}_1 \cdot \mathbf{I} \mathbf{E}_2 (2 \mathbf{I} \mathbf{E}_1 \cdot \mathbf{X}_I - 2 \mathbf{I} \mathbf{E}_1 \cdot \mathbf{X}_J + \mathbf{I} \mathbf{E}_1 \cdot \mathbf{J} \mathbf{E}_2 (-\mathbf{J} \mathbf{E}_2 \cdot \mathbf{X}_I \right. \\ & \left. + \mathbf{J} \mathbf{E}_2 \cdot \mathbf{X}_J) \right) \Big) \Big) / \Omega, \tag{117} \end{aligned}$$

$$\begin{aligned} \alpha_1^k = & \left(3 \left(-2 (-4 + (\mathbf{I} \mathbf{E}_1 \cdot \mathbf{J} \mathbf{E}_2)^2) (\mathbf{J} \mathbf{E}_1 \cdot \mathbf{X}_I - \mathbf{J} \mathbf{E}_1 \cdot \mathbf{X}_J) + \right. \right. \\ & \mathbf{I} \mathbf{E}_1 \cdot \mathbf{J} \mathbf{E}_2 (-\mathbf{I} \mathbf{E}_1 \cdot \mathbf{X}_I + \mathbf{I} \mathbf{E}_1 \cdot \mathbf{X}_J) \mathbf{J} \mathbf{E}_1 \cdot \mathbf{I} \mathbf{E}_2 \mathbf{I} \mathbf{E}_2 \cdot \mathbf{J} \mathbf{E}_2 \\ & + (\mathbf{J} \mathbf{E}_1 \cdot \mathbf{J} \mathbf{E}_2)^2 \mathbf{J} \mathbf{E}_1 \cdot \mathbf{I} \mathbf{E}_2 (\mathbf{J} \mathbf{E}_2 \cdot \mathbf{X}_I - \mathbf{I} \mathbf{E}_2 \cdot \mathbf{X}_J) + \\ & 4 \mathbf{J} \mathbf{E}_1 \cdot \mathbf{I} \mathbf{E}_2 (-\mathbf{I} \mathbf{E}_2 \cdot \mathbf{X}_I + \mathbf{I} \mathbf{E}_2 \cdot \mathbf{X}_J) \\ & + \mathbf{I} \mathbf{E}_1 \cdot \mathbf{J} \mathbf{E}_1 \left(\mathbf{I} \mathbf{E}_1 \cdot \mathbf{X}_I (-4 + (\mathbf{I} \mathbf{E}_2 \cdot \mathbf{J} \mathbf{E}_2)^2) - \right. \\ & \left. \mathbf{I} \mathbf{E}_1 \cdot \mathbf{X}_J (-4 + (\mathbf{I} \mathbf{E}_2 \cdot \mathbf{J} \mathbf{E}_2)^2) \right. \\ & \left. + \mathbf{I} \mathbf{E}_1 \cdot \mathbf{J} \mathbf{E}_2 \left(\mathbf{I} \mathbf{E}_2 \cdot \mathbf{J} \mathbf{E}_2 (-\mathbf{I} \mathbf{E}_2 \cdot \mathbf{X}_I + \mathbf{I} \mathbf{E}_2 \cdot \mathbf{X}_J) + \right. \right. \\ & \left. \left. 2 (\mathbf{J} \mathbf{E}_2 \cdot \mathbf{X}_I - \mathbf{J} \mathbf{E}_2 \cdot \mathbf{X}_J) \right) \right) + 2 \mathbf{I} \mathbf{E}_2 \cdot \mathbf{J} \mathbf{E}_2 \\ & \times \left((-\mathbf{J} \mathbf{E}_1 \cdot \mathbf{X}_I + \mathbf{J} \mathbf{E}_1 \cdot \mathbf{X}_J) \mathbf{I} \mathbf{E}_2 \cdot \mathbf{J} \mathbf{E}_2 + \right. \\ & \left. \mathbf{J} \mathbf{E}_1 \cdot \mathbf{I} \mathbf{E}_2 (\mathbf{J} \mathbf{E}_2 \cdot \mathbf{X}_I - \mathbf{J} \mathbf{E}_2 \cdot \mathbf{X}_J) \right) \Big) / \Omega, \tag{118} \end{aligned}$$

$$\begin{aligned} \alpha_2^k = & \left(3 \left(\mathbf{I} \mathbf{E}_1 \cdot \mathbf{J} \mathbf{E}_1 (-\mathbf{I} \mathbf{E}_1 \cdot \mathbf{X}_I + \mathbf{I} \mathbf{E}_1 \cdot \mathbf{X}_J) \mathbf{J} \mathbf{E}_1 \cdot \mathbf{I} \mathbf{E}_2 \mathbf{I} \mathbf{E}_2 \cdot \mathbf{J} \mathbf{E}_2 + \right. \right. \\ & \mathbf{I} \mathbf{E}_1 \cdot \mathbf{J} \mathbf{E}_2 \left(\mathbf{I} \mathbf{E}_1 \cdot \mathbf{X}_I (-4 + (\mathbf{J} \mathbf{E}_1 \cdot \mathbf{I} \mathbf{E}_2)^2) \right. \\ & \left. - \mathbf{I} \mathbf{E}_1 \cdot \mathbf{X}_J (-4 + (\mathbf{J} \mathbf{E}_1 \cdot \mathbf{I} \mathbf{E}_2)^2) + \right. \\ & \left. \mathbf{I} \mathbf{E}_1 \cdot \mathbf{J} \mathbf{E}_1 \left(2 \mathbf{J} \mathbf{E}_1 \cdot \mathbf{X}_I - 2 \mathbf{J} \mathbf{E}_1 \cdot \mathbf{X}_J + \mathbf{J} \mathbf{E}_1 \cdot \mathbf{I} \mathbf{E}_2 (-\mathbf{I} \mathbf{E}_2 \cdot \mathbf{X}_I + \right. \right. \\ & \left. \left. \mathbf{I} \mathbf{E}_2 \cdot \mathbf{X}_J) \right) \right) + (\mathbf{J} \mathbf{E}_1 \cdot \mathbf{J} \mathbf{E}_1)^2 (\mathbf{I} \mathbf{E}_2 \cdot \mathbf{J} \mathbf{E}_2 (\mathbf{I} \mathbf{E}_2 \cdot \mathbf{X}_I - \mathbf{I} \mathbf{E}_2 \cdot \mathbf{X}_J) \\ & - 2 \mathbf{J} \mathbf{E}_2 \cdot \mathbf{X}_I + 2 \mathbf{J} \mathbf{E}_2 \cdot \mathbf{X}_J) + \\ & 2 (\mathbf{J} \mathbf{E}_1 \cdot \mathbf{I} \mathbf{E}_2 (\mathbf{J} \mathbf{E}_1 \cdot \mathbf{X}_I - \mathbf{J} \mathbf{E}_1 \cdot \mathbf{X}_J) \mathbf{I} \mathbf{E}_2 \cdot \mathbf{J} \mathbf{E}_2 \\ & + 2 \mathbf{I} \mathbf{E}_2 \cdot \mathbf{J} \mathbf{E}_2 (-\mathbf{I} \mathbf{E}_2 \cdot \mathbf{X}_I + \mathbf{I} \mathbf{E}_2 \cdot \mathbf{X}_J) + \\ & \left. \left. 4 (\mathbf{J} \mathbf{E}_2 \cdot \mathbf{X}_I - \mathbf{J} \mathbf{E}_2 \cdot \mathbf{X}_J) + (\mathbf{J} \mathbf{E}_1 \cdot \mathbf{I} \mathbf{E}_2)^2 (-\mathbf{J} \mathbf{E}_2 \cdot \mathbf{X}_I + \mathbf{J} \mathbf{E}_2 \cdot \mathbf{X}_J) \right) \right) / \Omega, \tag{119} \end{aligned}$$

where Ω is

$$\Omega = \left((t_0 - t_1) \left((-4 + (\mathbf{I} \mathbf{E}_1 \cdot \mathbf{J} \mathbf{E}_2)^2) (-4 + (\mathbf{J} \mathbf{E}_1 \cdot \mathbf{I} \mathbf{E}_2)^2) - \right. \right. \\ \left. \left. 2 \mathbf{I} \mathbf{E}_1 \cdot \mathbf{J} \mathbf{E}_1 \mathbf{I} \mathbf{E}_1 \cdot \mathbf{J} \mathbf{E}_2 \mathbf{J} \mathbf{E}_1 \cdot \mathbf{I} \mathbf{E}_2 \mathbf{I} \mathbf{E}_2 \cdot \mathbf{J} \mathbf{E}_2 - \right. \right.$$

$$4 \left({}_J E_2 \cdot {}_J E_2 \right)^2 + \left({}_J E_1 \cdot {}_J E_1 \right)^2 \left(-4 + \left({}_J E_2 \cdot {}_J E_2 \right)^2 \right) \right). \quad (120)$$

A.3. Interpolation functions

The interpolation functions in (48)–(50), which stem from the cubic Hermite edge curves and the bilinear Coons patch, have the following form:

$${}_1 N_1(\xi^1, \xi^2) = -\frac{1}{8}(\xi^1 - 1)(\xi^2 - 1)(-2 + \xi^1 + (\xi^1)^2 + \xi^2 + (\xi^2)^2), \quad (121)$$

$${}_2 N_1(\xi^1, \xi^2) = \frac{1}{8}(\xi^1 + 1)(\xi^2 - 1)(-2 - \xi^1 + (\xi^1)^2 + \xi^2 + (\xi^2)^2),$$

$${}_3 N_1(\xi^1, \xi^2) = -\frac{1}{8}(\xi^1 + 1)(\xi^2 + 1)(-2 - \xi^1 + (\xi^1)^2 - \xi^2 + (\xi^2)^2),$$

$${}_4 N_1(\xi^1, \xi^2) = \frac{1}{8}(\xi^1 - 1)(\xi^2 + 1)(-2 + \xi^1 + (\xi^1)^2 - \xi^2 + (\xi^2)^2),$$

$${}_1 N_2(\xi^1, \xi^2) = -\frac{1}{8}(\xi^1 - 1)^2(\xi^1 + 1)(\xi^2 - 1), \quad (122)$$

$${}_2 N_2(\xi^1, \xi^2) = -\frac{1}{8}(\xi^1 + 1)^2(\xi^1 - 1)(\xi^2 - 1),$$

$${}_3 N_2(\xi^1, \xi^2) = \frac{1}{8}(\xi^1 + 1)^2(\xi^1 - 1)(\xi^2 + 1),$$

$${}_4 N_2(\xi^1, \xi^2) = \frac{1}{8}(\xi^1 - 1)^2(\xi^1 + 1)(\xi^2 + 1),$$

$${}_1 N_3(\xi^1, \xi^2) = -\frac{1}{8}(\xi^1 - 1)(\xi^2 - 1)^2(\xi^2 + 1), \quad (123)$$

$${}_2 N_3(\xi^1, \xi^2) = \frac{1}{8}(\xi^1 + 1)(\xi^2 - 1)^2(\xi^2 + 1),$$

$${}_3 N_3(\xi^1, \xi^2) = \frac{1}{8}(\xi^1 + 1)(\xi^2 + 1)^2(\xi^2 - 1),$$

$${}_4 N_3(\xi^1, \xi^2) = -\frac{1}{8}(\xi^1 - 1)(\xi^2 + 1)^2(\xi^2 - 1).$$

References

- [1] J.C. Simo, D.D. Fox, M.S. Rifai, On a stress resultant geometrically exact shell model. Part III: The linear theory, *Comput. Asp. Comput. Methods Appl. Mech. Eng.* 73 (1989) 53–92.
- [2] B. Brank, D. Perić, F.B. Damjanić, On large deformations of thin elasto-plastic shells: Implementation of a finite rotation model for quadrilateral shell element, *Internat. J. Numer. Methods Engrg.* 40 (1997) 281–306.
- [3] G.M. Kulikov, S.V. Plotnikova, A family of ANS four-node exact geometry shell elements in general convected curvilinear coordinates, *Internat. J. Numer. Methods Engrg.* 83 (2010) 1376–1406.
- [4] M. Lavrenčić, B. Brank, Hybrid-mixed shell quadrilateral that allows for large solution steps and is low-sensitive to mesh distortion, *Comput. Mech.* 65 (2020) 177–192.
- [5] F. Gruttmann, W. Wagner, A linear quadrilateral shell element with fast stiffness computation, *Comput. Methods Appl. Mech. Engrg.* 194 (2005) 4279–4300.
- [6] Y. Vetyukov, Finite element modeling of Kirchhoff-Love shells as smooth material surfaces, *ZAMM J. Appl. Math. Mech.* 1 (2014) 150–163.
- [7] L. Greco, M. Cuomo, An implicit G1-conforming bi-cubic interpolation for the analysis of smooth and folded Kirchhoff-Love shell assemblies, *Comput. Methods Appl. Mech. Engrg.* 373 (2021) 113476.
- [8] G. Farin, *Curves and Surfaces for CAD - A Practical Guide*, Elsevier, 2002.
- [9] T.W. Sederberg, J. Zheng, A. Bakenov, A.H. Nasri, T-splines and T-NURCCs, *ACM Trans. Graph.* 22(3) (2003) 477–484.
- [10] M. Cuomo, L. Greco, An implicit strong G1-conforming formulation for the analysis of the Kirchhoff plate model, *Contin. Mech. Thermodyn.* 32 (2020) 621–645.
- [11] M. Cuomo, L. Greco, A quadrilateral G1-conforming finite element for the Kirchhoff plate model, *Comput. Methods Appl. Mech. Engrg.* 346 (2019) 913–951.
- [12] T.J.R. Hughes, J.A. Cottrell, Y. Bazilevs, Isogeometric analysis: CAD, finite elements, NURBS, exact geometry and mesh refinement, *Comput. Methods Appl. Mech. Engrg.* 194 (2005) 4135–4195.
- [13] J. Kiendl, K.U. Bletzinger, J. Linhard, R. Wüchner, Isogeometric shell analysis with Kirchhoff-Love elements, *Comput. Methods Appl. Mech. Engrg.* 198 (2009) 3902–3914.
- [14] J. Kiendl, K.U. Bletzinger, J. Linhard, R. Wüchner, The bending strip method for isogeometric analysis of Kirchhoff-Love shell structures comprised of multiple patches, *Comput. Methods Appl. Mech. Engrg.* 199 (2010) 2403–2416.
- [15] J.-L. Batoz, M.B. Tahar, Evaluation of a new quadrilateral thin plate bending element, *Internat. J. Numer. Methods Engrg.* 18 (1982) 1655–1677.
- [16] U. Bohinc, A. Ibrahimbegovic, B. Brank, Model adaptivity for finite element analysis of thin or thick plates based on equilibrated boundary stress resultants, *Eng. Comput.* 26 (1/2) (2009) 69–99.
- [17] U. Bohinc, B. Brank, A. Ibrahimbegovic, Discretization error for the Discrete Kirchhoff plate finite element approximation, *Comput. Methods Appl. Mech. Engrg.* 269 (2014) 415–436.
- [18] J.L. Batoz, C.L. Zheng, F. Hammadi, A quadrilateral G1-conforming finite element for the Kirchhoff plate model, *Internat. J. Numer. Methods Engrg.* 52 (2001) 615–630.
- [19] S. Jaamei, F. Frey, P. Jetteur, Nonlinear thin finite element with six degrees of freedom per node, *Comput. Methods Appl. Mech. Engrg.* 75 (1989) 251–266.
- [20] F. Damak, S. Abid, A. Gakwaya, G. Dhart, A formulation of the non linear discrete kirchhoff quadrilateral shell element with finite rotations and enchaned strains, *Rev. Eur. Élé. Finis* 14 (2005) 7–31.
- [21] P.M.A. Areias, J.H. Song, T. Belytschko, A finite-strain quadrilateral shell element based on discrete Kirchhoff-Love constraints, *Internat. J. Numer. Methods Engrg.* 64 (2005) 1166–1206.
- [22] J. Simo, On a stress resultant geometrically exact shell model. Part VII: Shell intersections with -DOF finite element formulations, *Comput. Methods Appl. Mech. Engrg.* 108 (1993) 319–339.
- [23] J.C. Simo, D.D. Fox, On a stress resultant geometrically exact shell model. Part I: Formulation and optimal parametrization, *Comput. Methods Appl. Mech. Engrg.* 72 (1989) 267–304.
- [24] A.E. Green, W. Zerna, *Theoretical Elasticity*, Dover Publications, 2012.
- [25] T. Veldin, B. Brank, M. Brojan, Computational finite element model for surface wrinkling of shells on soft substrates, *Commun. Nonlinear Sci. Numer. Simul.* 78 (2019) 104863.
- [26] T. Veldin, M. Lavrenčić, B. Brank, M. Brojan, A comparison of computational models for wrinkling of pressurized core-shell systems, *Int. J. Non-Linear Mech.* 4 (2020) 1–5.
- [27] G. Jaklič, E. Žagar, Curvature variation minimizing cubic Hermite interpolants, *Appl. Math. Comput.* 218 (2011) 3918–3924.
- [28] J.H. Yong, F. Cheng, Geometric Hermite curves with minimum strain energy, *Comput. Aided Geom. Design* 21 (2004) 281–301.
- [29] M. Lavrenčić, B. Brank, Hybrid-mixed low-order finite elements for geometrically exact shell models: Overview and comparison, *Arch. Comput. Methods Eng.* 28 (2021) 1–35.
- [30] B. Brank, A. Ibrahimbegović, On the relation between different parametrizations of finite rotations for shells, *Eng. Comput.* 7 (2001) 950–973.
- [31] A. Ibrahimbegovic, B. Brank, P. Courtois, Stress resultant geometrically exact form of classical shell model and vector-like parameterization of constrained finite rotations, *Internat. J. Numer. Methods Engrg.* 52 (2001) 1235–1252.
- [32] H. Roh, M. Cho, The application of geometrically exact shell elements to B-spline surfaces, *Comput. Methods Appl. Mech. Engrg.* 193 (2004) 2261–2299.
- [33] A.A. Groenwold, N. Stander, An efficient 4-node 24 D.O.F. thick shell finite element with 5-point quadrature, *Eng. Comput.* 12 (1995) 723–747.
- [34] I. Wolfram Research: *Mathematica*, Version 11.3. 2018, Champaign.
- [35] J. Korelc, P. Wriggers, *Automation of Finite Element Methods*, Springer International Publishing, 2016.
- [36] J. Korelc, *AceFEM*, 2020, available at <http://syamech.fgg.uni-lj.si/>.
- [37] E. Dvorkin, K.J. Bathe, A continuum mechanics based four-node shell element for general nonlinear analysis, *Eng. Comput.* 1 (1984) 77–88.
- [38] R. Macneal, R. Harden, A proposed standard set of problems to test finite element accuracy, *Finite Elem. Anal. Des.* 1 (1) (1985) 3–20.
- [39] M. Lavrenčić, B. Brank, Simulation of shell buckling by implicit dynamics and numerically dissipative schemes, *Thin-Walled Struct.* 132 (2018) 682–699.
- [40] B. Brank, F.B. Damjanić, D. Perić, On implementation of a nonlinear four node shell finite element for thin multilayered elastic shells, *Comput. Mech.* 16 (5) (1995) 341–359.
- [41] Y. Ko, Y. Lee, P.S. Lee, K. Bathe, Performance of the MITC3+ and MITC4+ shell elements in widely-used benchmark problems, *Comput. Struct.* 193 (2017) 187–206.
- [42] B. Brank, A. Ibrahimbegović, U. Bohinc, On discrete-kirchhoff plate finite elements: Implementation and discretization error, in: H. Altenbach, G. Mikhasev (Eds.), *Shell and Membrane Theories in Mechanics and Biology: From Macro- to Nanoscale Structures*, Springer International Publishing, Switzerland, 2015, pp. 109–131.
- [43] Y. Ko, P.S. Lee, K.J. Bathe, The MITC4+ shell element in geometric nonlinear analysis, *Comput. Struct.* 185 (2017) 1–14.
- [44] A. Stanić, B. Brank, J. Korelc, On path-following methods for structural failure problems, *Comput. Mech.* 58 (2016) 281–306.
- [45] M. Brojan, D. Terwagne, R. Lagrange, P. Reis, Wrinkling crystallography on spherical surfaces, *Proc. Natl. Acad. Sci. USA* 122 (2015) 14–19.